ARL-TR-8603 • JAN 2019

US Army Research Laboratory

Green's Function Extraction from Atmospheric Acoustic Propagation

by Sandra L Collier, Max F Denis, John M Noble,
WC Kirkpatrick Alberts, II, David A Ligon, Leng K Sim,
Deryck D James, Christian G Reiff, and Jericho E Cain

Approved for public release; distribution is unlimited.

NOTICES

Disclaimers

ARL-TR-8603 ● JAN 2019

US Army Research Laboratory

Green's Function Extraction from Atmospheric Acoustic Propagation

by Sandra L Collier, Max F Denis, John M Noble, David A Ligon, Deryck D James, and Jericho E Cain
Computational and Information Sciences Directorate, ARL

WC Kirkpatrick Alberts, II, Leng K Sim, and Christian G Reiff
Sensors and Electron Devices Directorate, ARL

REPORT DOCUMENTATION PAGE	*Form Approved* *OMB No. 0704-0188*

1. REPORT DATE *(DD-MM-YYYY)* January 2019

2. REPORT TYPE Director's Research Initiative

3. DATES COVERED (From - To) October 2015–March 2018

4. TITLE AND SUBTITLE Green's Function Extraction from Atmospheric Acoustic Propagation

5a. CONTRACT NUMBER

5b. GRANT NUMBER

5c. PROGRAM ELEMENT NUMBER

6. AUTHOR(S) Sandra L Collier, Max F Denis, John M Noble, WC Kirkpatrick Alberts, II, David A Ligon, Leng K Sim, Deryck D James, Christian G Reiff, and Jericho E Cain

5d. PROJECT NUMBER DRI15-CI-062

5e. TASK NUMBER

5f. WORK UNIT NUMBER

7. PERFORMING ORGANIZATION NAME(S) AND ADDRESS(ES)
US Army Research Laboratory
ATTN: RDRL-CIE-S
Adelphi, MD 20783-1138

8. PERFORMING ORGANIZATION REPORT NUMBER ARL-TR-8603

9. SPONSORING/MONITORING AGENCY NAME(S) AND ADDRESS(ES)

10. SPONSOR/MONITOR'S ACRONYM(S)

11. SPONSOR/MONITOR'S REPORT NUMBER(S)

12. DISTRIBUTION/AVAILABILITY STATEMENT Approved for public release; distribution is unlimited.

13. SUPPLEMENTARY NOTES primary author's email: <sandra.l.collier4.civ@mail.mil>

14. ABSTRACT

A multiyear research project was conducted to determine the feasibility of using time reversal in conjunction with flow reversal, or similar signal processing methods, to extract the Green's function for outdoor sound propagation using sources in audible frequency ranges. Here we report the findings of this three-year Director's Research Initiative project. We present comparisons of the Green's function retrieval methods for an outdoor acoustic propagation channel by multidimensional deconvolution and cross correlation for different source waveforms. Of particular interest is the accuracy of the retrieved Green's function of a nonimpulsive sound source compared to that of an impulsive sound source. The retrieved Green's functions are used to estimate the pressure field response and compared to the actual measured response. The corresponding correlation coefficient and other measures are used to quantify the performance. To this end, outdoor acoustic experiments were conducted in an open field and forested area in southern Maryland. Results are presented for various source–receiver ranges up to 600 m.

15. SUBJECT TERMS impulse response function, outdoor sound propagation, atmospheric turbulence, wave propagation, Green's function, inhomogeneous media, cross correlation, multidimensional deconvolution, time reversal, phase conjugation

16. SECURITY CLASSIFICATION OF:			17. LIMITATION OF ABSTRACT	18. NUMBER OF PAGES	19a. NAME OF RESPONSIBLE PERSON
					Sandra L Collier
a. REPORT	b. ABSTRACT	c. THIS PAGE			19b. TELEPHONE NUMBER (Include area code)
Unclassified	Unclassified	Unclassified	UU	61	301-394-2641

Standard Form 298 (Rev. 8/98)
Prescribed by ANSI Std. Z39.18

Contents

List of Figures v

List of Tables vii

Acknowledgments viii

1. Introduction 1

2. Theory 4

2.1 Time Reversal for a Stationary Medium 4

2.2 Flow Reversal for a Moving Medium 7

3. Green's Function Estimators 11

3.1 Response Function for a General Source 11

3.2 Cross-Correlation Estimation 13

3.3 Multidimensional Deconvolution Estimation 14

3.4 Signal Processing and Performance Criteria 15

4. Experiments 16

4.1 Array Designs and Instrumentation 16

4.2 Atmospheric Conditions 18

5. Proof of Concept 23

6. Green's Function Retrieval: Propagation Distances $\leq$ 400 m 26

7. Green's Function Retrieval: Propagation Distances > 400 m 35

8. Green's Function Retrieval: Influence of Source Distribution 38

9. Conclusions 42

10. Metrics 43

11. References 45

List of Symbols, Abbreviations, and Acronyms **50**

Distribution List **51**

List of Figures

Fig. 1 Impulse response for a source originating at $(\mathbf{r}_0, t_0)$ and observed at $(\mathbf{r}, t)$ (green) and at $(\mathbf{r}', t')$ (blue), and CC between these observations (teal)....5

Fig. 2 Combination of a forward-propagating wave (blue) and backward-propagating wave (green) results in a virtual source at $(\mathbf{r}, t)$ (teal) that has an impulse response that is equivalent to CC provided that the Green's function of the backward-propagating wave is equivalent to the time-reversed Green's function 6

Fig. 3 Coordinate system for acoustic wave equations 8

Fig. 4 Percent difference between the Green's function using flow and time reversal (g^{FR}) and using only time reversal (g^{TR}) in the frequency domain 10

Fig. 5 Real and imaginary components of the Green's function using flow and time reversal (g^{FR}) and using only time reversal (g^{TR}) in the time domain 11

Fig. 6 Experimental sites at Blossom Point for a) an open field and b) a forested area (images: Google Earth) 16

Fig. 7 Instrumentation. Upper: two-axis array (left); three-axis array and sonic anemometer (right). Lower: propane cannon and speaker (left and center); met tower with Airmars (right). 17

Fig. 8 Doppler lidar measured horizontal wind speed, wind direction, wind shear, and turbulence as a function of time and height AGL for 13 Sep 2016. The red brackets indicate the time frame during which the acoustic data are analyzed. 20

Fig. 9 Horizontal Doppler lidar scan at ground level for 14 Sep 2016....21

Fig. 10 von Kármán turbulence observations for 30 Aug 2017 using sonic data: power spectral density of turbulence (upper center); u, v, w wind measurements (left column); temperature, wind speed, and wind direction (right column)....22

Fig. 11 Estimated Green's function between channel 2 of the receiving array and channels 1–4 of the transmitting array for 20 pulses generated with a propane cannon....24

Fig. 12 Comparison of the predicted signals using the retrieved Green's function (blue) and the measured signal (red) between channel 2 of both the receiving and transmitting array 25

Fig. 13 Comparison of the theoretical Green's function for unbounded propagation derived using only time reversal and FR for the atmospheric conditions corresponding to Figs. 11 and 12 26

Fig. 14 Experimental setup: a) open field 13–14 Sep 2016 and b) forested area 15–16 Sep 2016 (images: Google Earth) 27

Fig. 15 Typical received signals (normalized) measured in the open field at the 10-m reference microphone (top row) and corresponding power spectral density (bottom row) 28

Fig. 16 Spectrogram of propane cannon measured in the open field: (upper left) unfiltered and (lower left) filtered reference signals; (upper right) 100-m array and (lower right) 400-m array filtered signals 29

Fig. 17 Retrieved Green's functions for a propane cannon in the a) open field and b) forested area between like elements ($\nu = l$) of arrays A and B. CC method is red and MDD is blue 30

Fig. 18 Spectrograms for nonimpulsive source S_1, S_2, and S_3 measured in the open field. For each source: (upper left) unfiltered and (lower left) filtered reference signals; (upper right) 100-m array and (lower right) 400-m array filtered signals 31

Fig. 19 CC (upper) and MDD Green's function (lower) retrievals for nonimpulsive sources (left) foghorn S_1, (center) twirl S_2, and (right) decompression S_3 between arrays $A = 100\,\mathrm{m}$ and $B = 400\,\mathrm{m}$ in the open field 32

Fig. 20 Spectrograms for nonimpulsive source S_1, S_2, and S_3 measured in the forest. For each source: (upper left) unfiltered and (lower left) filtered reference signals; (upper right) 100-m array and (lower right) 300-m array filtered signals. 33

Fig. 21 MDD Green's function retrievals for nonimpulsive sources (left) foghorn S_1, (center) twirl S_2, and (right) decompression S_3 measured in the forest between arrays $A = 100\,\mathrm{m}$ and $B = 300\,\mathrm{m}$ 34

Fig. 22 Estimated response $p_\delta(\mathbf{r}_\nu^A, t) * \hat{G}_\delta^{\mathrm{CC,MDD}}(\mathbf{r}_l^B, \mathbf{r}_\nu^A; t)$ compared with measured response $p_\delta(\mathbf{r}_l^B, t)$ for a propane cannon detected at $A = 100\,\mathrm{m}$ and $B = 400\,\mathrm{m}$ in the open field 34

Fig. 23 Estimated response $p_\delta(\mathbf{r}_\nu^A, t) * \hat{G}_\delta^{\mathrm{CC,MDD}}(\mathbf{r}_l^B, \mathbf{r}_\nu^A; t)$ compared with measured response $p_\delta(\mathbf{r}_l^B, t)$ for a propane cannon detected at $A = 100\,\mathrm{m}$ and $B = 300\,\mathrm{m}$ in the forested area 35

Fig. 24 Experimental setup for long-range propagation tests (image: Google Earth) 36

Fig. 25 Long-range propagation Green's function retrieval using propane cannon: (left) CC and (right) MDD 37

Fig. 26 Long-range propagation estimated response $p_\delta(\mathbf{r}_\nu^A, t) * \hat{G}_\delta^{\mathrm{CC,MDD}}(\mathbf{r}_l^B, \mathbf{r}_\nu^A; t)$ compared with measured response $p_\delta(\mathbf{r}_l^B, t)$ for a propane cannon shot detected at $A = 400\,\mathrm{m}$ and $B = 600\,\mathrm{m}$ 37

Fig. 27 Long-range propagation MDD Green's function retrieval for nonimpulsive sources S_1, S_2, and S_3 38

Fig. 28 Long-range propagation estimated response $p_{S_i}(\mathbf{r}_l^A, t) * G_{S_i}^{\mathrm{MDD}}(\mathbf{r}_l^B, \mathbf{r}_l^A; t)$ compared with measured response $p_{S_i}(\mathbf{r}_l^B, t)$ for nonimpulsive sources S_1, S_2, and S_3 detected at $A = 400\,\mathrm{m}$ and $B = 600\,\mathrm{m}$ 38

Fig. 29 Experimental setups with varying source-to-array center radii (images: Google Earth) 39

Fig. 30 Normalized pressure responses for sources considered in the source distribution study: a) propane cannon, b) foghorn S_1, and c) broadband source S_4 40

Fig. 31 Retrieved Green's function for $r_\odot = 500\,\mathrm{m}$ for the source waveforms: a) MDD and CC propane cannon Green's function, and the MDD recorded signal S_1 Green's function, and b) MDD and CC propane cannon Green's function, and the MDD recorded signal S_4 Green's function. Estimated response $p_\delta(\mathbf{r}_\nu^A, t) * \hat{G}_\delta(\mathbf{r}_l^B, \mathbf{r}_\nu^A; t)$ (red) and measured response $p_\delta(\mathbf{r}_l^B; t)$ (blue) for the propane cannon using the c) CC and d) MDD methods for the maximum correlation coefficient cases, $\rho_{\max,\delta}^{\mathrm{CC}} = 0.92$ and $\rho_{\max,\delta}^{\mathrm{MDD}} = 0.96$, respectively. 41

List of Tables

Table 1 Atmospheric data averaged over the time frame of the experimental analysis 19

Table 2 Varying source distribution: correlation coefficient median and IQR statistics for MDD and CC Green's function retrieval: δ propane cannon, S_1 foghorn, and S_4 broadband. CC only given for the propane cannon. 27

Acknowledgments

This research was supported in part by an appointment to the US Army Research Laboratory Research Associateship Program administered by Oak Ridge Associated Universities.

1. Introduction

Acoustic waves propagating in the atmosphere may undergo many effects, to include refraction by temperature and wind velocity gradients, scattering by atmospheric turbulence, absorption by the atmosphere (fluid), diffraction by terrain features, and absorption and reflection by a porous ground. As a result, there may be insonification in acoustic shadow zones, amplitude and phase fluctuations of the propagating sound signals, loss of signal coherence, changes in the interference maxima and minima of the direct ground reflected waves, and multipath effects. Understanding these effects is important for a variety of military applications, such as acoustic source localization and classification, noise propagation in the atmosphere, and the development of new remote sensing techniques of the atmosphere. These topics continue to be of high interest, particularly for impulse propagation.[1–4]

By extracting the medium impulse response, or Green's function, one may obtain information about the medium channel in order to overcome the medium effects or deduce information about the medium. For example, in acoustic communications, information is sent through a medium from a host station to client stations. The transmitted information is subjected to a variety of signal distortions and noise caused by the medium. Using time-reversal processing, Candy *et al.*[5–7] extracted the channel medium impulse response from the transmission of a known pilot signal through the channel medium. This Green's function was then used to modify the subsequent signals to overcome distortion in the channel.

Motivation for the current research is partially derived from atmospheric acoustic communications; however, time-reversal techniques are used in numerous fields far too extensive to summarize here. In optics, phase conjugation, the frequency-domain equivalent of time reversal, is often used; time-reverse mirrors and cavities are other examples. Ultrasound, geophysics, underwater acoustics, and communications are yet more examples of fields where time reversal is employed. Significant progress has been made in ultrasound. The pivotal and extensive body of work by Fink has impacted all these fields. References 5–51 only represent a very small fraction of the body of work in the literature. Of particular interest are the ultrasound/biomedical research of Xu and Wang[27] and Thomas *et al.*[24] and the underwater acoustic communications research that considers complex propagation effects by Fink[12] and Kuperman *et al.*[14] Seismic interferometry is another method used to estimate Green's functions between receivers. A 2011 special issue of *Earthquake Science* on earthquake geodesy summarizes many applications of this topic (preface, Ni[17]), and Wapenaar and colleagues[8,9] have several significant findings and summary articles.

Marengo and Gruber[15] proposed and demonstrated a coherent detection scheme based on time-reversal mirrors and cavities where propagation is governed by the optical theorem for wavefields (e.g., electromagnetic, optical, and acoustic in certain media). The optical theorem is well known to describe energy conservation for scattering systems. They sought to detect scatterers embedded in reciprocal media. They found good results for target detection in complex, highly reverberant environments, such as within buildings, urban canyons, tunnels, and caves. The performance was found to decrease when noise significantly corrupted the background signal estimation.

Time reversal has been successful for source localization and medium imaging, yet much of the research requires spatial reciprocity and temporal invariance. These assumptions are often invalid for moving media and absorptive media. This is critical when considering atmospheric acoustic propagation. A key finding of many of the investigations is that time reversal is more successful when there is considerable multipath.

For diffuse media, it has been demonstrated that cross correlation (CC) of two recordings of the diffuse wave field at different receivers can be used to retrieve the Green's function between these receivers. The theory was extended to include cases where time-reversal invariance and spatial reciprocity do not hold (e.g., Slob *et al.*[19] and Snieder[20]). The use of passive field fluctuations instead of an active point source has also been considered, where not only is the retrieval of the difference of the Green's function and its time-reversed function considered, but the sum is as well (Snieder *et al.*[21]). This formalism leads to applications for field fluctuations in static systems for potential field problems and direct current problems in conducting media, as well as for diffusive fields excited by injection sources or current sources. A unified theory was developed for Green's function retrieval when time-reversal invariance does not hold (Wapenaar *et al.*[44]).

Land mine detection exploits the highly elastically nonlinear property of land mines. Sutin *et al.*[22,23] successfully performed land mine detection by using a nonlinear distortion of a highly focused time-reversed acoustic signal. The method was based on time-reversal techniques from the ultrasound community. The nonlinear acoustic method uses the excitation of two frequency waves that interact with the top surface of the mine. The mine and the ground near the mine have different vibration frequencies, thus this method allows detection near other dense material, such as isolated cobbles.

While time reversal and similar methods have been used for Green's function estimation in many disciplines, there is little research for sound fields in the atmosphere. The use of noise interferometry to deduce wind velocity and sound speed has been studied by Godin and colleagues[30,31] and time reversal for source localization in urban environments is presented in Refs. 32–36. The potential impact for acoustic intelligence, surveillance, and reconnaissance (ISR) applications in the atmosphere warrants further investigation into Green's function estimation and, motivated by the large successes in other fields, has led to the development of this multiyear Director's Research Initiative research project.

The objective of this project is to determine the feasibility of using time reversal in conjunction with flow reversal, or other similar methods, to extract a Green's function for outdoor acoustic propagation using sources in audible frequency ranges. Several propagation factors unique to acoustic propagation in the atmosphere must be considered. First, inherent in the assumptions used in many time-reverse methods is that the medium is stationary. For moving media, a flow-reversal theorem may be used in conjunction with time reversal. Second, spatial reciprocity may not be valid due to terrain features or atmospheric conditions. Multidimensional deconvolution (MDD) has been successful for use in lossless media with homogeneous illumination of all receivers;[47–49] for some atmospheric conditions, this may provide an alternative retrieval method. Unlike previous research in other fields, the concept for this project is for military applications. Sources of opportunity (such as bell towers or fog horns) or limited active sources (such as a propane cannon) are considered, as well as limited acoustic sensor arrays. In theater, full illumination of all receivers is not a realistic scenario. However, such retrieval methods may provide sufficient information under certain environmental conditions.

In Section 2, we review the basic concept of time reversal in the context of estimating the Green's function for acoustic propagation. Flow reversal for a moving medium is also presented and typical cases for sound propagation in the atmosphere are examined to determine when incorporation of flow reversal into Green's function estimation becomes important. Two Green's function estimators are then derived in Section 3, a CC method, inspired by the work of Candy *et al.*,[5–7] and a MDD method, inspired by the work of Wapenaar *et al.*[44] Experiments were conducted to investigate Green's function estimation. An overview of the experimental site, array designs, and instrumentation, as well as the atmospheric conditions during the tests, is given in Section 4, The initial proof of concept is presented in Section 5. Sections 6, 7, and 8 examine the Green's function retrievals for open field and forested propagation up to 400 m, longer-range open field propagation up to 600 m, and the effect of source distribution, respectively. Finally, concluding remarks are given in Section 9.

2. Theory

In this section, we briefly review the concepts behind simple time reversal in a time-invariant and spatially reciprocal medium. We then introduce the concept of flow reversal in the context of wave propagation in a random medium. We explore cases relevant to acoustic propagation in the atmosphere in order to determine conditions under which flow reversal should be considered.

2.1 Time Reversal for a Stationary Medium

Consider a simplified case, as depicted in Fig. 1. An impulse originates at time t_0 and location $\mathbf{r}_0$. It then propagates to receiving location $\mathbf{r}$, arriving at time t. The Green's function $g(\mathbf{r}, t; \mathbf{r}_0, t_0)$ (green) is the impulse response between $(\mathbf{r}_0, t_0)$ and $(\mathbf{r}, t)$. The signal further propagates and is observed at a later time t' and location $\mathbf{r}'$. The Green's function between the point of origin $(\mathbf{r}_0, t_0)$ and later reception $(\mathbf{r}', t')$ is $g(\mathbf{r}', t'; \mathbf{r}_0, t_0)$ (blue). The paths associated with $g(\mathbf{r}, t; \mathbf{r}_0, t_0)$ and $g(\mathbf{r}', t'; \mathbf{r}_0, t_0)$ have the path from $\mathbf{r}_0$ and $\mathbf{r}$ in common. The travel time for this common path will cancel during CC (teal). Hence the CC of responses at $(\mathbf{r}, t)$ and $(\mathbf{r}', t')$ is equivalent to the response function $g(\mathbf{r}', t'; \mathbf{r}, t)$ for a source that initiates at $(\mathbf{r}, t)$ and is received at $(\mathbf{r}', t')$.

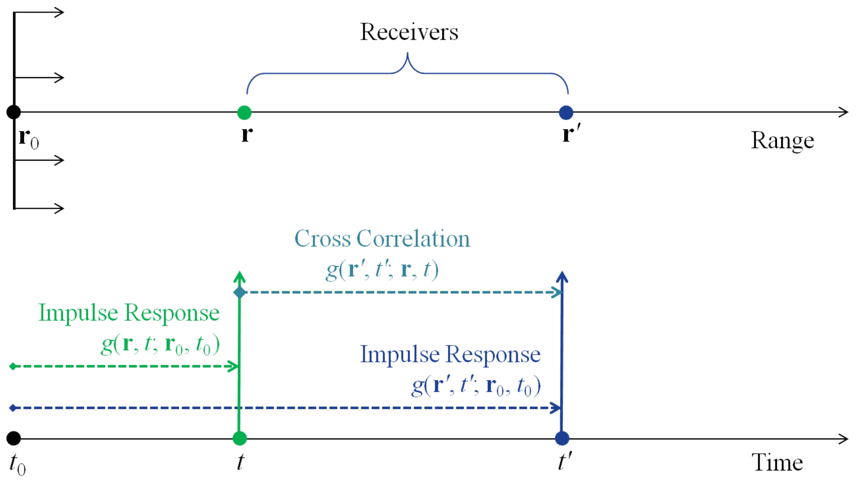

Fig. 1 Impulse response for a source originating at $(\mathbf{r}_0, t_0)$ and observed at $(\mathbf{r}, t)$ (green) and at $(\mathbf{r}', t')$ (blue), and CC between these observations (teal)

Since the paths between times $(\mathbf{r}, t)$ and $(\mathbf{r}', t')$ are the same for both receivers, we can equivalently consider the coherent sum of a forward-propagating wave between $\mathbf{r}_0$ and $\mathbf{r}$ (blue) and a backward-propagating wave between $\mathbf{r}'$ and $\mathbf{r}$ (green), as shown in Fig. 2. This backward-propagating wave may be thought of as a time-reversed signal provided the Green's function for the time-reversed signal and the backward-propagating wave, which are the same. Therefore, time reversal holds provided $g(\mathbf{r}_0, t_0; \mathbf{r}, t) = g(\mathbf{r}, -t; \mathbf{r}_0, t_0)$, so that

$$g(\mathbf{r}', t'; \mathbf{r}, t) = g(\mathbf{r}', t'; \mathbf{r}_0, t_0) * g(\mathbf{r}, -t'; \mathbf{r}_0, t_0). \tag{1}$$

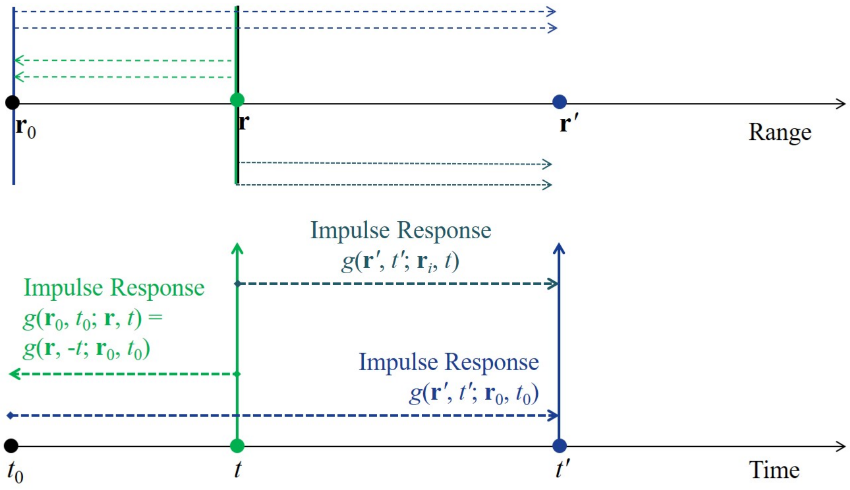

Fig. 2 Combination of a forward-propagating wave (blue) and backward-propagating wave (green) results in a virtual source at $(\mathbf{r}, t)$ (teal) that has an impulse response that is equivalent to CC provided that the Green's function of the backward-propagating wave is equivalent to the time-reversed Green's function

Thus, the impulse response function between $(\mathbf{r}, t)$ and $(\mathbf{r}', t')$ (teal) is equivalent to the CC and is given by the convolution

$$\begin{aligned} g(\mathbf{r}', t'; \mathbf{r}, t) &= g(\mathbf{r}', t'; \mathbf{r}_0, t_0) * g(\mathbf{r}, -t'; \mathbf{r}_0, t_0) \\ &= \int g(\mathbf{r}', \tau; \mathbf{r}_0, t_0) g(\mathbf{r}, t' + \tau; \mathbf{r}_0, t_0) d\tau. \end{aligned} \tag{2}$$

The receiver located at $\mathbf{r}$ can be thought of as a virtual source. Similarly for full 3-D propagation, a receiver array can be viewed as an array of virtual sources. These concepts are used in many applications, such as seismic interferometry and communications.[5–9] This concept holds when there are both temporal invariance and spatial reciprocity.

As an example, consider 1-D propagation in free space. For an impulse emitted at time t_0 and location x_0, observed at time t and location x, the causal 1-D Green's function for free space is

$$g(x, t; x_0, t_0) = \delta\left(|t - t_0| - \frac{|x - x_0|}{c_0}\right), \tag{3}$$

where c_0 is the sound speed. Thus, the Green's function between the two observations (x,t) and (x',t') is given by

$$\begin{aligned} g(x',t';x,t) &= g(x',t';x_0,t_0) \ast g(x,-t';x_0,t_0) \\ &= \int g(x',\tau;x_0,t_0) g(x,\tau+t';x_0,t_0) d\tau \\ &= \int \delta\left(|\tau-t_0| - \frac{|x'-x_0|}{c_0}\right)\delta\left(|\tau+t'-t_0| - \frac{|x-x_0|}{c_0}\right)d\tau \\ &= \delta\left(|t'| - \frac{|x'-x|}{c_0}\right), \end{aligned} \tag{4}$$

and we recover the known causal solution.

2.2 Flow Reversal for a Moving Medium

The atmosphere is a moving, random medium and, in general, acoustic propagation in the atmosphere violates the assumptions of the previous subsection. The complete set of fluid dynamics equations for sound propagation in the atmosphere may be written as[3,37,38]

$$\left(\frac{\partial}{\partial t} + \mathbf{v}\cdot\boldsymbol{\nabla}\right)p + \rho c^2 \boldsymbol{\nabla}\cdot\mathbf{w} = \rho c^2 Q, \tag{5}$$

$$\left(\frac{\partial}{\partial t} + \mathbf{v}\cdot\boldsymbol{\nabla}\right)\mathbf{w} + (\mathbf{w}\cdot\boldsymbol{\nabla})\,\mathbf{v} + \frac{\boldsymbol{\nabla}p}{\rho} = \frac{\mathbf{F}}{\rho}, \tag{6}$$

where $p(\mathbf{r},t)$ is the acoustic pressure, $\mathbf{w} = \mathbf{w}(\mathbf{r},t)$ the acoustic particle velocity, $\mathbf{v} = \mathbf{v}(\mathbf{r},t)$ the ambient medium velocity, $\rho = \rho(\mathbf{r},t)$ the medium density, $c = c(\mathbf{r},t)$ the sound speed in the medium, $Q = Q(\mathbf{r},t)$ the mass source term, and $\mathbf{F} = \mathbf{F}(\mathbf{r},t)$ the external force. For a uniform medium with uniform flow velocity (*i.e.*, c, ρ, and $\mathbf{v}$ are independent of $\mathbf{r}$ and t), this simplifies to

$$\left(\frac{1}{c}\frac{\partial}{\partial t} - \frac{\mathbf{v}\cdot\boldsymbol{\nabla}}{c}\right)^2 p - \boldsymbol{\nabla}^2 p = \rho\left[\left(\frac{\partial}{\partial t} + \mathbf{v}\cdot\boldsymbol{\nabla}\right)Q - \boldsymbol{\nabla}\cdot\mathbf{F}\right], \tag{7}$$

and the corresponding Green's function $g(t,\mathbf{r};t_0,\mathbf{r}_0)$ is given by

$$\left(\frac{1}{c}\frac{\partial}{\partial t} - \frac{\mathbf{v}\cdot\boldsymbol{\nabla}}{c}\right)^2 g - \boldsymbol{\nabla}^2 g = \delta(t-t_0)\delta(\mathbf{r}-\mathbf{r}_0). \tag{8}$$

Without loss of generality, consider the 2-D case, where $\mathbf{v} = v\hat{\mathbf{e}}_x$ and $\mathbf{r} = (x,y) = (r\cos\varphi, r\sin\varphi)$, as shown in Fig. 3. The Green's function is given by

$$\left(\frac{1}{c}\frac{\partial}{\partial t}-\frac{v}{c}\frac{\partial}{\partial x}\right)^2 g-\left(\frac{\partial^2}{\partial x^2}+\frac{\partial^2}{\partial y^2}\right) g=\delta(t-t_0)\delta(x-x_0)\delta(y-y_0). \tag{9}$$

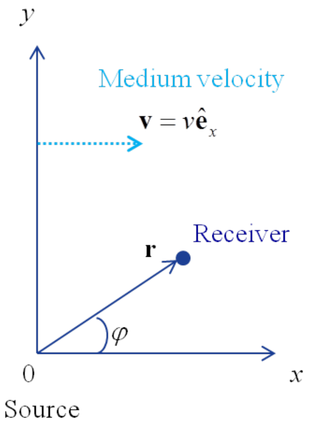

Fig. 3 Coordinate system for acoustic wave equations

This can be solved by Fourier transforming to the frequency domain ω, where we use the convention

$$g(\mathbf{r},t)=\frac{1}{\sqrt{2\pi}}\int_{-\infty}^{\infty}\tilde{g}(\mathbf{r},\omega)e^{-i\omega t}d\omega \quad \text{and} \quad \tilde{g}(\mathbf{r},\omega)=\frac{1}{\sqrt{2\pi}}\int_{-\infty}^{\infty}g(\mathbf{r},t)e^{i\omega t}dt. \tag{10}$$

Without loss of generality, let $t_0=0$ and $\mathbf{r}_0=0$. Then

$$-k^2\tilde{g}-2iMk\frac{\partial\tilde{g}}{\partial x}+M^2\frac{\partial^2\tilde{g}}{\partial x^2}-\frac{\partial^2\tilde{g}}{\partial x^2}-\frac{\partial^2\tilde{g}}{\partial y^2}=\frac{\delta(x)\delta(y)}{\sqrt{2\pi}}, \tag{11}$$

which has the solution

$$\begin{aligned}\tilde{g}(\mathbf{r},\omega;0,0)=&\frac{i}{2\,(2\pi)^{1/2}\,(1-M^2)^{3/2}}\left[H_0^{(1)}(k\rho)-\frac{iMx}{\rho\,(1-M^2)}H_1^{(1)}(k\rho)\right]\times\\ &\exp\left(\frac{-ikxM}{1-M^2}\right),\end{aligned} \tag{12}$$

where the wave number, Mach speed, and scaled range are respectively given by

$$k = \frac{\omega}{c}, \quad M = \frac{v}{c}, \quad \text{and} \quad \rho = \left\{ \frac{1}{1-M^2} \left[\frac{x^2}{1-M^2} + y^2 \right] \right\}^{1/2}. \tag{13}$$

Time reversal corresponds to phase conjugation in the frequency domain. Therefore, the time-reversed signal is given by

$$g^{\mathrm{TR}}(\mathbf{r}, t; 0, 0) = \frac{1}{\sqrt{2\pi}} \int_{-\infty}^{\infty} \tilde{g}^{\mathrm{TR}}(\mathbf{r}, \omega; 0, 0) e^{-i\omega t} d\omega, \tag{14}$$

where

$$\begin{aligned} &\tilde{g}^{\mathrm{TR}}(\mathbf{r}, \omega; 0, 0) = \tilde{g}^{*}(\mathbf{r}, \omega; 0, 0) \\ &= \frac{-i}{2\,(2\pi)^{1/2}\,(1-M^2)^{3/2}} \left[H_0^{(2)}(k\rho) + \frac{iMx}{\rho\,(1-M^2)} H_1^{(2)}(k\rho) \right] \exp\left(\frac{ikxM}{1-M^2} \right), \end{aligned} \tag{15}$$

and the dependence of k on ω is implicit.

For a moving medium, $M \neq 0$, a time-reversed signal and a backward-propagating wave are not the same. Therefore, it is necessary to incorporate both time reversal (phase conjugation) and flow reversal ($M \to -M$). Now we must explicitly denote the dependence of the Green's function on the parameter M. Therefore, letting "FR" denote both time and flow reversal, we have

$$g^{\mathrm{FR}}(\mathbf{r}, t; 0, 0; M) = \frac{1}{\sqrt{2\pi}} \int_{-\infty}^{\infty} \tilde{g}^{\mathrm{FR}}(\mathbf{r}, \omega; 0, 0; M) e^{-i\omega t} d\omega, \tag{16}$$

where

$$\begin{aligned} &\tilde{g}^{\mathrm{FR}}(\mathbf{r}, \omega; 0, 0; M) = \tilde{g}^{*}(\mathbf{r}, \omega; 0, 0; -M) \\ &= \frac{-i}{2\,(2\pi)^{1/2}\,(1-M^2)^{3/2}} \left[H_0^{(2)}(k\rho) - \frac{iMx}{\rho\,(1-M^2)} H_1^{(2)}(k\rho) \right] \exp\left(\frac{-ikxM}{1-M^2} \right). \end{aligned} \tag{17}$$

To quantify the significance of flow reversal for atmospheric acoustic propagation, let us consider some typical cases. Figure 4 shows the percent difference in the magnitudes of $\tilde{g}^{\mathrm{FR}}$ and $\tilde{g}^{\mathrm{TR}}$ as a function of frequency ω. Ranges of 10 m (upper left), 100 m (upper right), 1,000 m (lower left), and 10,000 m (lower right) are considered for on-axis propagation ($\varphi = 0$) and a characteristic sound speed of 340 m/s. The blue lines are for a wind speed of 1 m/s, green 5 m/s, red 10 m/s, cyan 15 m/s, and magenta 100 m/s. For the last case, $v/c \not\ll 1$ is outside the range of validity of Eqs. 5 and 6; however, it allows us to examine the limiting behavior. We see that the largest percent difference is for values of $\omega < 1$, and for larger ω, the percent difference approaches a limit. The largest percent difference occurs at values that have a smaller weight in the Fourier transform, the smaller v/c, the smaller the weight. This is evident in Fig. 5, which shows the real and imaginary components of the Green's functions in the time domain, here for a range of 100 m. Blue is the real component of g^{TR}, red the imaginary of g^{TR}, green the real of g^{FR}, and cyan the imaginary of g^{FR}. For $v = 1$ m/s, we see that there is little difference. As v increases, we notice a change in the magnitude and phase, and the incorporation of flow reversal becomes more important. Again, $v = 100$ m/s is outside the range of validity of the model, but shows the limiting behavior. Further detailed analysis reveals that when $v/c \gtrsim 0.015$, flow reversal should be considered.

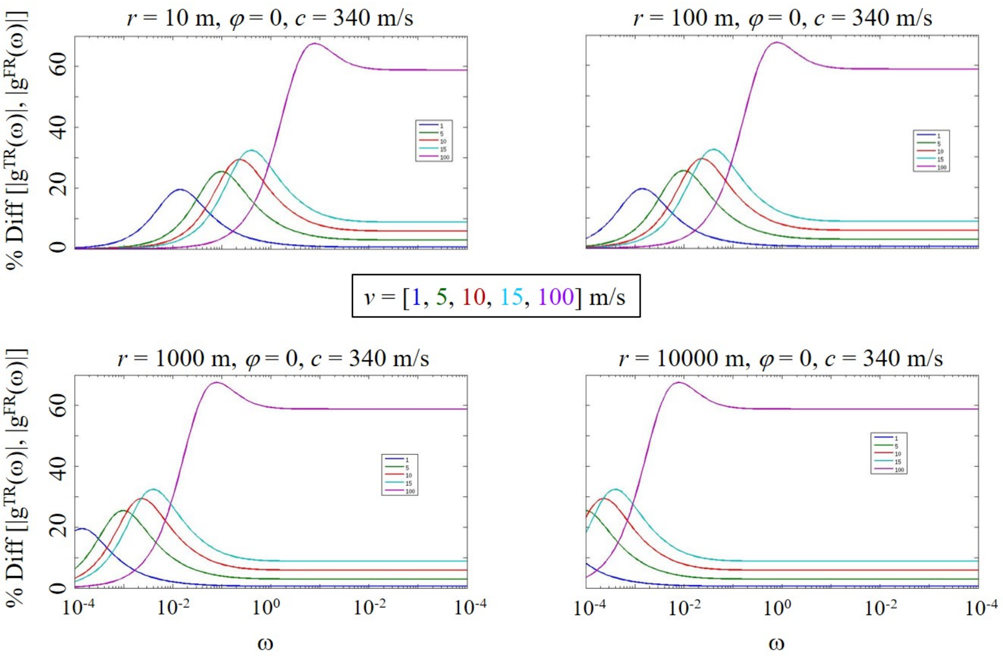

Fig. 4 Percent difference between the Green's function using flow and time reversal (g^{FR}) and using only time reversal (g^{TR}) in the frequency domain

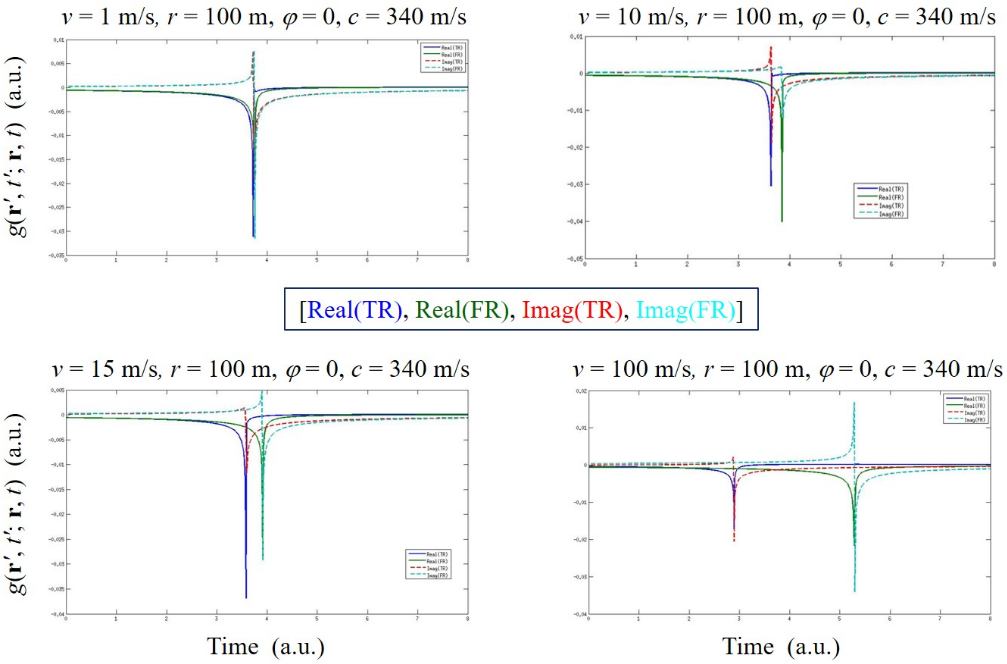

Fig. 5 Real and imaginary components of the Green's function using flow and time reversal (g^{FR}) and using only time reversal (g^{TR}) in the time domain

3. Green's Function Estimators

As previously discussed, the Green's function is the medium response function to a delta function source. This is physically unrealizable. Therefore, in this section, we discuss the medium response function for a general source and develop two Green's function estimations techniques: CC and MDD.

3.1 Response Function for a General Source

Let us now generalize the concept of the medium impulse response in Section 2 to that of a medium response function for a general source.

Consider a general time-dependent, stationary source $s(t, t_0, \mathbf{r}_0)$ that initiates at time t_0 and location $\mathbf{r}_0$. The medium response function $u(\mathbf{r}, t; \mathbf{r}_0, t_0)$ is given by the convolution

$$u(\mathbf{r}, t; \mathbf{r}_0, t_0) = g(\mathbf{r}, t; \mathbf{r}_0, t_0) * s(t, t_0, \mathbf{r}_0). \tag{18}$$

Thus, for the two points of observation $(\mathbf{r}_i, t_i)$ and $(\mathbf{r}'_j, t'_j)$, assuming time reversal holds,

$$\begin{aligned}
u(\mathbf{r}'_j, t'_j; \mathbf{r}_i, t_i) &= u(\mathbf{r}'_j, t'_j; \mathbf{r}_0, t_0) * u(\mathbf{r}_i, -t'_j; \mathbf{r}_0, t_0) \\
&= \left[g(\mathbf{r}'_j, t'_j; \mathbf{r}_0, t_0) * s(t'_j, t_0, \mathbf{r}_0)\right] * \left[g(\mathbf{r}_i, -t'_j; \mathbf{r}_0, t_0) * s(-t'_j, t_0, \mathbf{r}_0)\right] \\
&= \left[g(\mathbf{r}'_j, t'_j; \mathbf{r}_0, t_0) * g(\mathbf{r}_i, -t'_j; \mathbf{r}_0, t_0)\right] * \left[s(t'_j, t_0, \mathbf{r}_0) * s(-t'_j, t_0, \mathbf{r}_0)\right] \\
&= g(\mathbf{r}'_j, t'; \mathbf{r}_i, t_i) * S(t'_j, t_0, \mathbf{r}_0). \qquad (19)
\end{aligned}$$

Here the autocorrelation function of the source observed at t'_j is

$$S(t'_j, t_0, \mathbf{r}_0) = s(t'_j, t_0, \mathbf{r}_0) * s(-t'_j, t_0, \mathbf{r}_0), \qquad (20)$$

and the convolution with the time-reversed function is the CC

$$\begin{aligned}
g(\mathbf{r}'_j, t'_j; \mathbf{r}_0, t_0) * g(\mathbf{r}_i, -t'_j; \mathbf{r}_0, t_0) &= \int g(\mathbf{r}'_j, \tau; \mathbf{r}_0, t_0) g(\mathbf{r}_i, t'_j + \tau; \mathbf{r}_0, t_0) d\tau \\
&= g(\mathbf{r}'_j, t'_j; \mathbf{r}_i, t_i). \qquad (21)
\end{aligned}$$

Experimentally, the estimate of the response function $\hat{u}(\mathbf{r}'_j, t'_j; \mathbf{r}_i, t_i)$ may be determined from the convolution of the measured signal z at $\mathbf{r}'_j$ with the time-reverse measured signal x at $\mathbf{r}_i$, which may be written in terms of the Green's functions:

$$\begin{aligned}
\hat{u}(\mathbf{r}'_j, t'_j; \mathbf{r}_i, t_i) &\approx z(\mathbf{r}'_j, t'_j; \mathbf{r}_0, t_0) * x(\mathbf{r}_i, -t'_j; \mathbf{r}_0, t_0) \\
&\approx \left[g(\mathbf{r}'_j, t'_j; \mathbf{r}_0, t_0) * g(\mathbf{r}_i, -t'_j; \mathbf{r}_0, t_0)\right] * S(t'_j, t_0, \mathbf{r}_0). \qquad (22)
\end{aligned}$$

If the autocorrelation function of the source approaches a delta function

$$S(t'_j, t_0, \mathbf{r}_0) \to \delta(t'_j - t_0), \qquad (23)$$

then the estimated Green's function $\hat{g}$ approaches the estimated response function

$$\begin{aligned}
\hat{g}(\mathbf{r}'_j, t'_j; \mathbf{r}_i, t_i) \to \hat{u}(\mathbf{r}'_j, t'_j; \mathbf{r}_i, t_i) &\approx z(\mathbf{r}'_j, t'_j; \mathbf{r}_0, t_0) * x(\mathbf{r}_i, -t'_j; \mathbf{r}_0, t_0) \\
&\to g(\mathbf{r}'_j, t'_j; \mathbf{r}_0, t_0) * g(\mathbf{r}_i, -t'_j; \mathbf{r}_0, t_0) \\
&\approx g(\mathbf{r}'_j, t'_j; \mathbf{r}_i, t_i). \qquad (24)
\end{aligned}$$

For simplicity, we write the Green's function estimate between the two receivers as

$$\hat{g}(\mathbf{r}'_j, t'_j; \mathbf{r}_i, t_i) = z(\mathbf{r}'_j, t'_j) * x(\mathbf{r}_i, -t'_j). \qquad (25)$$

This argument, which follows that of Candy *et al.*[5–7] for communications, is valid for signals that satisfy an impulsive-like autocorrelation function property and sample the medium only within the information bandwidth. Physically, the medium must be time invariant (or approximately so for the analysis window) and spatially reciprocal. In terms of seismic interferometry, it is used for lossless media and equipartitioned waves (receivers illuminated isotropically from all directions).

Physically, the autocorrelation function of the source will never be a delta function. In terms of battlefield sound sources, impulsive signals, such as gun shots and propane cannon shots, may provide a reasonable approximation. However, in general, we seek a solution for a more general source.

The MDD method is one method employed in seismics. It makes use of the point-spread function (PSF), by deconvolving the PSF from the estimated medium response function $\hat{u}$ (e.g., Wapenaar *et al.*[47]).

The next two subsections present, in terms of the measured acoustic pressure field, the two Green's function estimation techniques considered in this report.

3.2 Cross-Correlation Estimation

Without loss of generality, consider a source originating at $\mathbf{r}_0$ at time $t_0 = 0$. The CC of the received pressure signal $p\big(\mathbf{r}_l^B, t; \mathbf{r}_0\big)$ measured at element l of array B (located at $\mathbf{r}_l^B$) with the time-reversed received signal $p\big(\mathbf{r}_\nu^A, -t; \mathbf{r}_0\big)$ measured at element ν of array A (located at $\mathbf{r}_\nu^A$) is given by[5]

$$\begin{aligned} C\big(\mathbf{r}_l^B, \mathbf{r}_\nu^A; t\big) &= \big\langle p\big(\mathbf{r}_l^B, t; \mathbf{r}_0\big) * p\big(\mathbf{r}_\nu^A, -t; \mathbf{r}_0\big)\big\rangle \\ &= \big[G\big(\mathbf{r}_l^B, t; \mathbf{r}_0\big) * G\big(\mathbf{r}_\nu^A, -t; \mathbf{r}_0\big)\big] * S(t; \mathbf{r}_0)\,, \end{aligned} \tag{26}$$

where the brackets indicate ensemble average and, as before, $S(t; \mathbf{r}_0)$ is autocorrelation of the source function. If this approaches a delta function, $S(t; \mathbf{r}_0) \to \delta(t)$, then the estimated Green's function between $\mathbf{r}_l^B$ and $\mathbf{r}_\nu^A$ may be approximated as

$$\hat{G}^{\mathrm{CC}}(\mathbf{r}_l^B, \mathbf{r}_\nu^A; t) \approx C(\mathbf{r}_l^B, \mathbf{r}_\nu^A; t). \tag{27}$$

We refer to this as the CC Green's function estimation technique.

If the autocorrelation of the source is not approximately a delta function, then

$C(\mathbf{r}_l^B, \mathbf{r}_\nu^A; t)$ is an estimate of the response function of the medium. The Green's function could then be estimated by deconvolving $S(t; \mathbf{r}_0)$ from $C(\mathbf{r}_l^B, \mathbf{r}_\nu^A; t)$, provided that the autocorrelation function of the source is known. As it is often unknown, the MDD method is employed for a general source.

3.3 Multidimensional Deconvolution Estimation

Following the derivation of Wapenaar *et al.*,[47] the CC between two receiver locations may be written as

$$C(\mathbf{r}_l^B, \mathbf{r}_\nu^A; t) = 2 \int_\Omega G(\mathbf{r}_l^B, \mathbf{r}; t) \ast \Gamma(\mathbf{r}, \mathbf{r}_\nu^A; t) d\mathbf{r}, \tag{28}$$

where Γ is the PSF defined as

$$\Gamma(\mathbf{r}, \mathbf{r}_\nu^A; t) = \left\langle p(\mathbf{r}, t; \mathbf{r}_0) \ast p(\mathbf{r}_\nu^A, -t; \mathbf{r}_0) \right\rangle . \tag{29}$$

In practice, $C(\mathbf{r}_l^B, \mathbf{r}_\nu^A; t)$ and $\Gamma(\mathbf{r}_l^B, \mathbf{r}_\nu^A; t)$ are estimated in the time domain and then transformed to the frequency domain as $\tilde{C}(\mathbf{r}_l^B, \mathbf{r}_\nu^A; \omega)$ and $\tilde{\Gamma}(\mathbf{r}_l^B, \mathbf{r}_\nu^A; \omega)$, respectively. Assuming a number of sources exist on the surface Ω, Eq. 28 can be solved in a least-squares sense. Therefore, the system of equations for the inversion process may be written in the frequency domain as

$$\begin{bmatrix} \tilde{C}(\mathbf{r}_l^B, \mathbf{r}_1^A; \omega) \\ \tilde{C}(\mathbf{r}_l^B, \mathbf{r}_2^A; \omega) \\ \vdots \\ \tilde{C}(\mathbf{r}_l^B, \mathbf{r}_N^A; \omega) \end{bmatrix} = \begin{bmatrix} \tilde{\Gamma}(\mathbf{r}_1^A, \mathbf{r}_1^A; \omega) & \tilde{\Gamma}(\mathbf{r}_1^A, \mathbf{r}_2^A; \omega) & \dots & \tilde{\Gamma}(\mathbf{r}_1^A, \mathbf{r}_N^A; \omega) \\ \tilde{\Gamma}(\mathbf{r}_2^A, \mathbf{r}_1^A; \omega) & \tilde{\Gamma}(\mathbf{r}_2^A, \mathbf{r}_2^A; \omega) & \dots & \tilde{\Gamma}(\mathbf{r}_2^A, \mathbf{r}_N^A; \omega) \\ \vdots & \vdots & \ddots & \vdots \\ \tilde{\Gamma}(\mathbf{r}_N^A, \mathbf{r}_1^A; \omega) & \tilde{\Gamma}(\mathbf{r}_N^A, \mathbf{r}_2^A; \omega) & \dots & \tilde{\Gamma}(\mathbf{r}_N^A, \mathbf{r}_N^A; \omega) \end{bmatrix} \begin{bmatrix} \tilde{G}(\mathbf{r}_l^B, \mathbf{r}_1^A; \omega) \\ \tilde{G}(\mathbf{r}_l^B, \mathbf{r}_2^A; \omega) \\ \vdots \\ \tilde{G}(\mathbf{r}_l^B, \mathbf{r}_N^A; \omega) \end{bmatrix} . \tag{30}$$

Accordingly, we define $\tilde{\mathbf{\Gamma}}$ as a $N \times N$ matrix, and $\tilde{\mathbf{C}}$ and $\tilde{\mathbf{G}}$ as $N \times 1$ column vectors showing receiver gathers. The Green's function is estimated by matrix inversion

$$\tilde{\mathbf{G}} = \tilde{\mathbf{\Gamma}}^{-1} \tilde{\mathbf{C}}, \tag{31}$$

where $\tilde{\mathbf{\Gamma}}^{-1}$ is a generalized inverse of $\tilde{\mathbf{\Gamma}}$. It should be noted that the inversion process may suffer from ill-posed solutions. The damped least-squares method can be directly adapted to Eq. 31, yielding the frequency-domain MDD estimate of the Green's function

$$\tilde{\mathbf{G}}^{\mathrm{MDD}} = \left[\tilde{\mathbf{\Gamma}}^\dagger \tilde{\mathbf{\Gamma}} + \epsilon \mathbf{I} \right]^{-1} \tilde{\mathbf{\Gamma}}^\dagger \tilde{\mathbf{C}}, \tag{32}$$

where ϵ and $\mathbf{I}$ indicate a stabilization factor and the identity matrix, respectively. The MDD estimate of the Green's function in the time domain is thus

$$\hat{\mathbf{G}}^{\mathrm{MDD}} = \mathcal{F}^{-1}\left(\tilde{\mathbf{G}}^{\mathrm{MDD}}\right). \tag{33}$$

3.4 Signal Processing and Performance Criteria

The acoustic data processing is a multistep process. First, the recorded raw signal of interest is calibrated to a tone signal. Background noise reduction is then performed, typically using both a bandpass filter and Weiner filter. The filtered signal is then aligned using a matched filter with the reference signal and peak detection. The Green's function is then retrieved using the CC or MDD estimation technique previously presented.

The two performance criteria that we consider are the signal-to-noise ratio (SNR) and the correlation coefficient. Consider the function Φ that has spatial and temporal dependence. Following Kao *et al.*,[50] the SNR is defined by the ratio of the maximum amplitude of the function Φ divided by the mean value of the function:

$$\mathrm{SNR} = \frac{\max\left(\Phi\right)}{\mathrm{mean}\left(\Phi\right)}. \tag{34}$$

Now suppose we wish to compare Φ to another function Ψ. The Pearson correlation coefficient ρ is used as a measure of agreement between Φ and Ψ:

$$\rho = \frac{\langle \Phi\Psi \rangle - \langle \Phi \rangle \, \langle \Psi \rangle}{\sqrt{\left(\langle \Phi^2 \rangle - \langle \Phi \rangle^2\right)\left(\langle \Psi^2 \rangle - \langle \Psi \rangle^2\right)}}. \tag{35}$$

The median value and the interquartile range (IQR; 25th–75th percentile) of the correlation coefficients provide a quantitative measure: high median correlation coefficients ($\bar{\rho} > 0.5$) and low IQR values (signifying that most of the correlation coefficient values are close to the median) correspond to good performance.

4. Experiments

A series of outdoor experiments were conducted at Blossom Point, Maryland, during the summer to early-fall months between 2015 and 2017. This section provides a brief overview of the instrumentation and summarizes the measured atmospheric conditions for the cases considered herein.

4.1 Array Designs and Instrumentation

Figure 6 shows the open field and forested area where the experiments were conducted. All of these experiments utilized multiple microphone arrays, though each experiment had a unique array configuration. The open field is relatively flat and grassy, allowing easy emplacement of the arrays. The forested area has uneven, undulating ground. Due to the dense vegetation and trees, the microphone arrays were positioned in grassy areas on the side of gravel roads cutting through the forest.

Fig. 6 Experimental sites at Blossom Point for a) an open field and b) a forested area (images: Google Earth)

The instrumentation and microphone arrays are shown in Fig. 7. A variety of sources were used: propane cannon shots approximated impulses, and speakers broadcast broadband recorded signals, such as fog horns and church bells, and synthesized signals (using source generators), such as sawtooth and sine waves. Atmospheric data were collected from Airmar WeatherStations located on a meteorological (met) tower, Doppler wind lidars (not pictured) performed horizontal and vertical scans, and a sonic anemometer was located on the ground near one of the arrays.

Fig. 7 Instrumentation. Upper: two-axis array (left); three-axis array and sonic anemometer (right). Lower: propane cannon and speaker (left and center); met tower with Airmars (right).

The first experiment in June 2015 used L-shaped arrays (parallel to the ground) with four microphones arranged along the transverse direction and four microphones along the longitudinal direction. The remaining experiments used tri-axis arrays with four microphones along each axis. The adjacent element spacing for both the two- and three-axis arrays was 0.5 m. Brüel & Kjær microphones were used. Data acquisition was done using National Instruments CompactRIO with a NI 9239 analog input module with the sampling frequency set to 25 Hz. The experiments conducted in 2015 and 2016 (Sections 5, 6, and 8) used a specialized speaker,[52] a JBL 2446H pressure driver coupled to a 1-m-long pipe with a 3.175-cm inner diameter (this can be approximated as a point source to a frequency of roughly 2.7 kHz). The experiments in 2017 used Peavey Impulse 1015 loudspeakers. A bank of four speakers were used for the long-range experiment (Section 7), and single speakers were used for each station in the multisource experiment (Section 8).

To present the results in a consistent manner for the different experiments, we use the following conventions henceforth in this report. The Cartesian coordinates $\mathbf{r} = (x, y, z)$ are defined so that x is the longitudinal component (horizontal plane), y is the transverse component (horizontal plane), and z is the vertical component. The x-axis is also referred to as the propagation axis. All arrays use the same numbering convention for the microphone elements: elements 1–4 are in the horizontal plane transverse to the propagation axis (y), elements 5–8 are in the horizontal plane parallel to the propagation axis (x), and elements 9–12 are in the vertical direction orthogonal to the propagation axis (z). The exception is the multisource experiment, which is further described in Section 8.

4.2 Atmospheric Conditions

Horizontal wind speed, wind direction, temperature, barometric pressure, and relative humidity were measured with Airmars located on a nearby met tower. Two coherent Doppler wind lidars were located downrange from the source, collecting radial wind velocity data. One performed a vertical sweep to obtain profile data and the other performed a horizontal scan along the propagation path.

The average atmospheric data, collected on the lowest level Airmar during the course of the experiment, are summarized in Table 1 for the cases presented herein. The data are averaged over the analysis window. Overall, the wind speeds are low. The large variability in wind direction is commonly seen at low wind speeds and often represents instrumentation limitations. The largest value of the Mach speed, v/c, is less than 0.01; therefore, flow reversal need not be considered in our analyses. We also find that there is well-established von Kármán turbulence.

Table 1 Atmospheric data averaged over the time frame of the experimental analysis

Date	Environment	Temperature (C)	Humidity (%)	Wind speed (m/s)	Wind direction (°)	Sound speed (m/s)
13 Sep 2016	Open field	24.1 ± 0.1	70.6 ± 0.6	2.7 ± 0.6	233.0 ± 9.3	346.0 ± 0.1
14 Sep 2016	Open field	23.0 ± 0.1	77.5 ± 0.7	2.6 ± 0.4	273.0 ± 19.3	345.9 ± 0.1
15 Sep 2016	Forest	22.9 ± 0.2	63.7 ± 0.5	2.2 ± 0.8	67.2 ± 36.8	345.7 ± 0.1
16 Sep 2016	Forest	24.0 ± 0.5	58.8 ± 2.2	1.3 ± 0.7	118.0 ± 69.0	346.0 ± 0.3
30 Aug 2017	Open field	20.6 ± 3.3	66.1 ± 3.7	2.5 ± 0.1	188.0 ± 108.0	
1 Sep 2017	Open field	17.9 ± 0.3	66.7 ± 0.8	3.0 ± 1.1	58.4 ± 94.0	

As an example of observed lidar data, consider the open field experiment 13–14 Sep 2016. The horizontal wind speed and direction measured with a coherent Doppler lidar (Halo Photonics: Streamline) are shown in the upper half of Fig. 8 for 13 Sep 2016. The acoustic data were collected between 1500 and 1800 Universal Coordinated Time (UTC) (local time: 1100 to 1400 Eastern Daylight Time), as indicated by the red brackets. We see that prior to the acoustic measurements, the atmosphere exhibited a low-level jet of moderate strength (≈ 12 m/s) at a height of 300 m above ground level (AGL) at about 0400 UTC. This structure eroded throughout the early morning and was gone by the start of the acoustic measurements. Overall, during the acoustic measurement collection, the wind speed was light with consistent direction. The vertical wind speed was negligible; therefore, it is not presented.

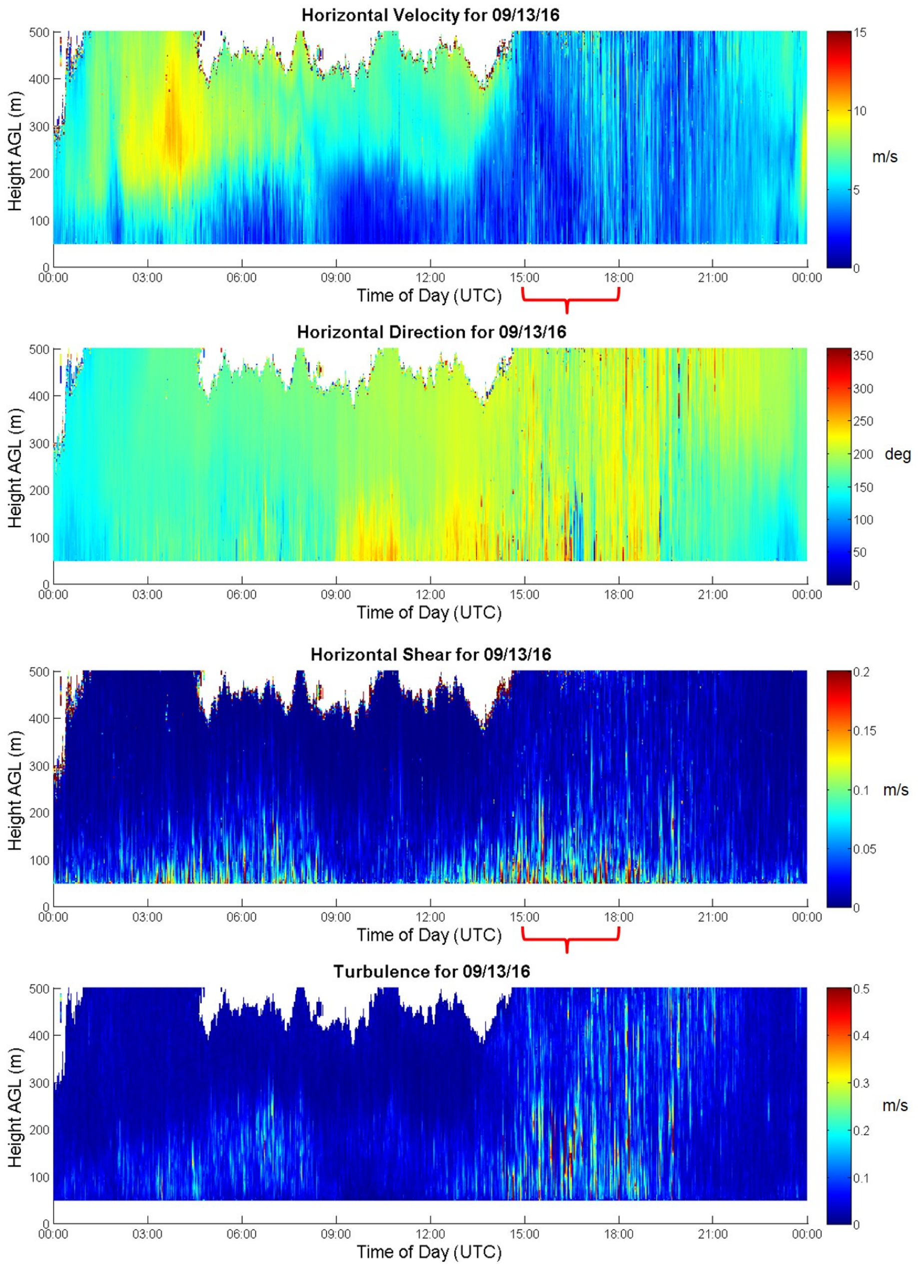

Horizontal Velocity for 09/13/16

Horizontal Direction for 09/13/16

Horizontal Shear for 09/13/16

Turbulence for 09/13/16

Fig. 8 Doppler lidar measured horizontal wind speed, wind direction, wind shear, and turbulence as a function of time and height AGL for 13 Sep 2016. The red brackets indicate the time frame during which the acoustic data are analyzed.

The horizontal wind shear and effective turbulence are shown in the lower half of Fig. 8. We can see that both horizontal wind shear and turbulence are low over the entire day of the test. There was increased wind direction variability over the following days.

A horizontal Doppler lidar scan is shown in Fig. 9 for 14 Sep 2016. The scan was done at 0° elevation, corresponding to roughly 0.5-m height AGL. The tree lines are clearly evident on the boundaries. There is a notable rolling structure due to winds.

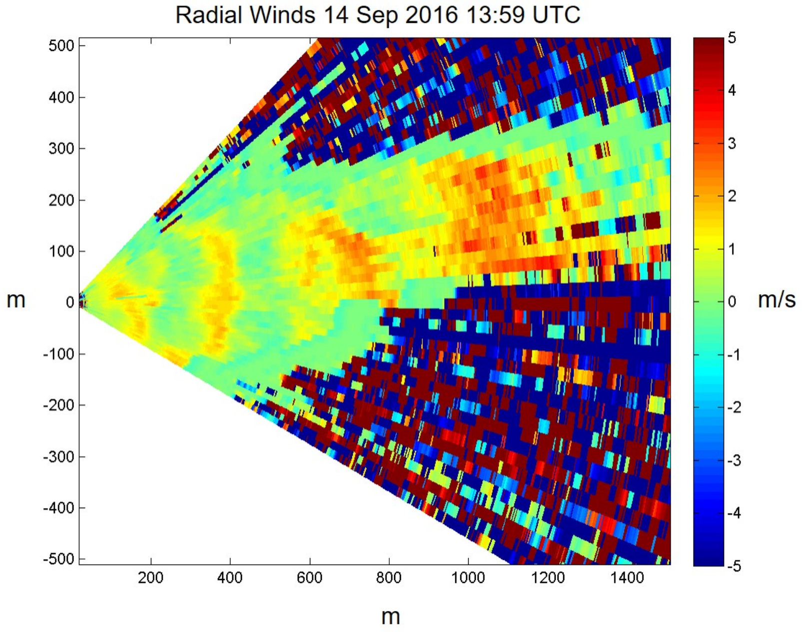

Fig. 9 Horizontal Doppler lidar scan at ground level for 14 Sep 2016

Figure 10 shows typical anemometer wind measurements for 30 Aug 2017. The u, v, w wind component measurements are in the left column, and the temperature, wind speed, and wind direction are in the right column. The high variability in wind direction corresponds to the lowest measured wind speeds. The uppermost centered plot shows the calculated power spectral density of the turbulence, which is clearly well described by a von Kármán model.

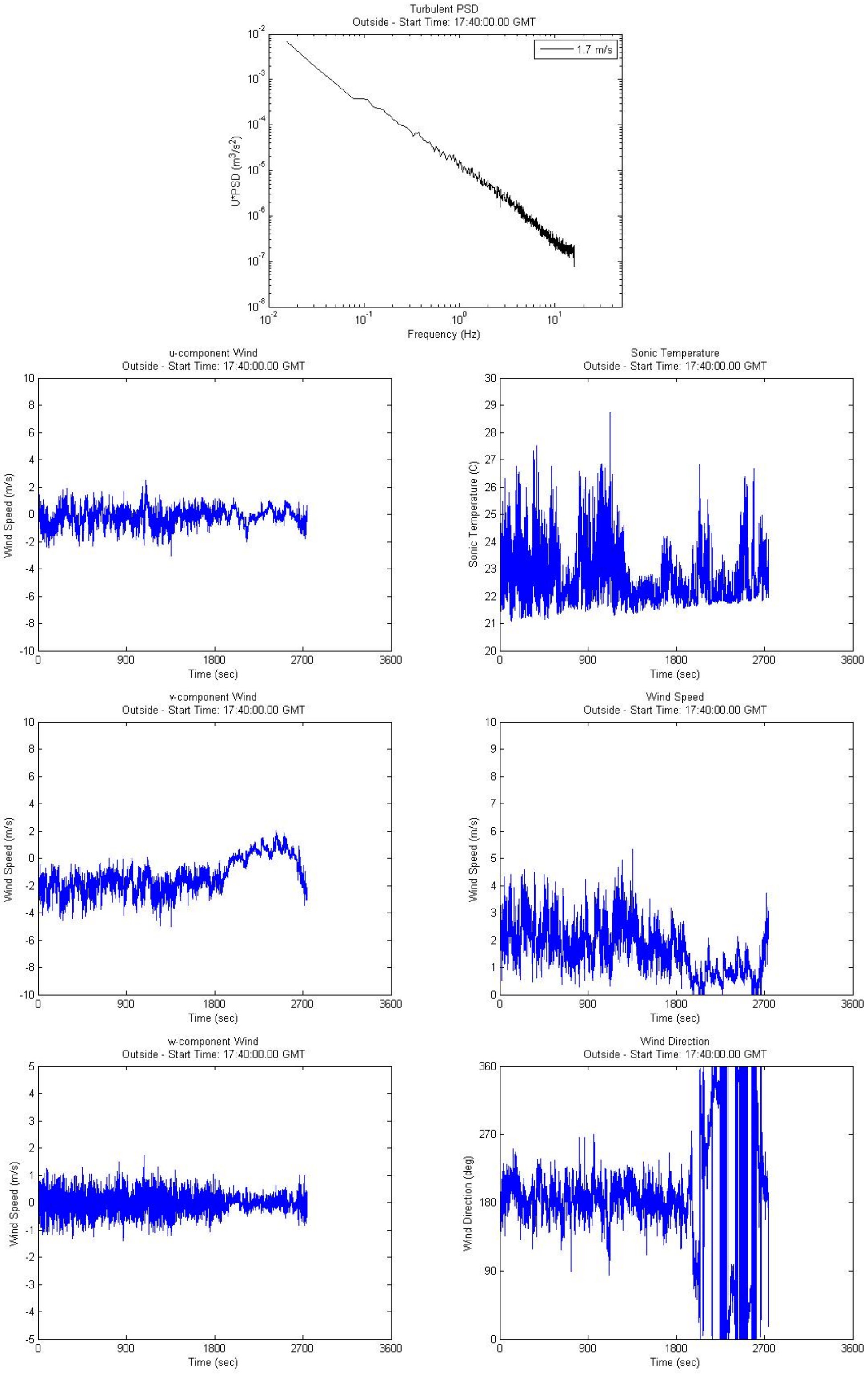

Fig. 10 von Kármán turbulence observations for 30 Aug 2017 using sonic data: power spectral density of turbulence (upper center); u, v, w wind measurements (left column); temperature, wind speed, and wind direction (right column)

5. Proof of Concept

We first demonstrate that the Green's function can be retrieved for outdoor sound propagation. For the proof-of-concept analysis, we consider acoustic data that were collected in the open field at Blossom Point, Maryland, in mid-June 2015. The warm weather ensured strong convectively driven turbulence. Five measurement sites were used: reference microphone at a 10-, 100-, 300-, 400-, and 500-m array. These eight-element L-shaped arrays were aligned on the propagation axis.

For the proof of concept, let us consider the pilot signal as that of the propane cannon. The signal satisfies the impulsive-like autocorrelation function property and samples the medium only within the information bandwidth. Therefore, we may use the CC Green's function estimator, $\hat{\mathbf{G}}^{\mathrm{CC}}$. A matched filter is used for time alignment.

As an example of the results using the CC estimator, consider the 100- and 500-m arrays, which may we may respectively think of as the transmitting and receiving arrays. The Green's function is estimated for 20 impulses generated with a propane cannon during a 10-min period. During this period, the average air temperature was 32.7 °C (91.1 °F), relative humidity was 54.0%, mean wind speed was 3.47 m/s, average wind direction was 267.4° with 270° being against the propagation direction, mean sound speed was 352.1 m/s, and mean effective sound speed was 349.7 m/s. There was well-defined von Kármán turbulence. Figure 11 presents the time-evolving Green's function for the transverse elements $l = 1,\ 2,\ 3,\ 4$ of the transmitting array and the transverse element $m = 2$ of the receiving array (each with uniform sensor spacing of 0.5 m). Four cases show minor deviations from the others, and these cases correspond to increased background noise—the closest approach of a lawn mower to the arrays. The reduced SNR for these cases may lead to errors in the matched filter alignment.

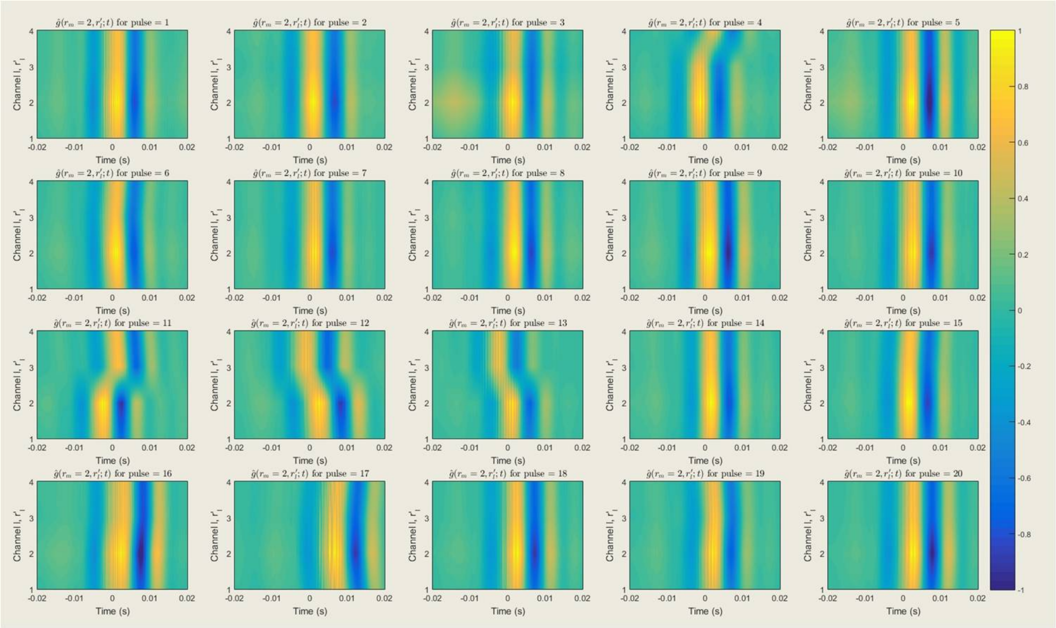

Fig. 11 Estimated Green's function between channel 2 of the receiving array and channels 1–4 of the transmitting array for 20 pulses generated with a propane cannon

Using the estimated Green's function for the first pulse, we can predict the received signal at the 500-m array based on the measured signal at the 100-m array for each of the 20 pulses. Figure 12 shows the results for channel 2 of both the transmitting and receiving arrays. Doing this, we find that the data for each pulse pass a χ^2 goodness of fit, and that the absolute value of the mean variance between the predicted and measured signal is less than 0.01 for each pulse.

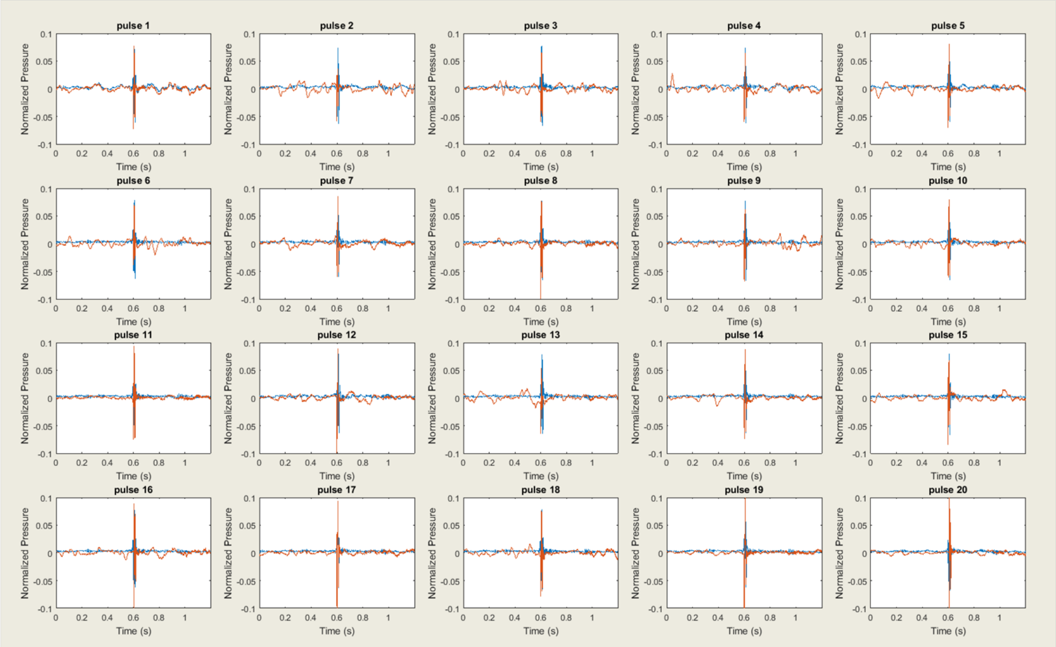

Fig. 12 Comparison of the predicted signals using the retrieved Green's function (blue) and the measured signal (red) between channel 2 of both the receiving and transmitting array

Finally, using the atmospheric data for this test, let us examine the impact of flow on the Green's function for unbounded atmospheric propagation. Figure 13 (left) presents the percent difference between the magnitudes of $\tilde{g}^{\mathrm{FR}}$ and $\tilde{g}^{\mathrm{TR}}$ in the frequency domain, for ranges corresponding to the sensor placements: blue 100 m, green 200 m, red 300 m, cyan 400 m, and purple 500 m. The largest percent difference occurs near $\omega \sim 10^{-2}$ for $r = 100\,\mathrm{m}$. Figure 13 (right) compares the real and imaginary components of g^{FR} and g^{TR} in the time domain for $r = 400\,\mathrm{m}$. There is a slight difference in the magnitudes and a slight shift in the phase. The estimated Green's function therefore deviates most from that of free space propagation due to the boundary conditions, not the medium flow. However, flow reversal may become more important when considering the Green's function with ground boundary conditions.

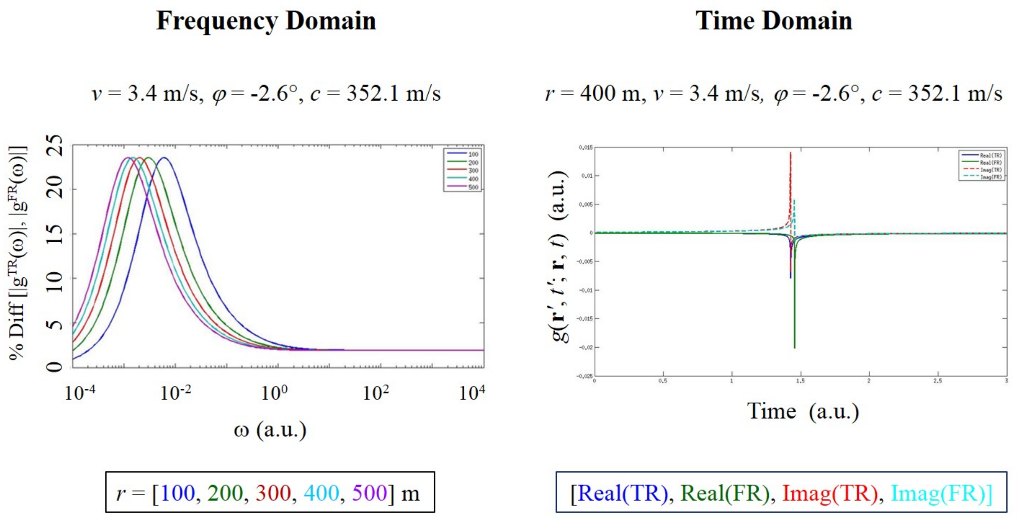

Fig. 13 Comparison of the theoretical Green's function for unbounded propagation derived using only time reversal and FR for the atmospheric conditions corresponding to Figs. 11 and 12

Having demonstrated that Green's function estimation for outdoor sound propagation is feasible, we now consider more in-depth estimation and applications using data from the subsequent experiments.

6. Green's Function Retrieval: Propagation Distances $\leq$ 400 m

We now examine the CC and MDD estimation techniques for both open field and forested propagation. For the analysis presented in this section, we consider propagation distances up to 400 m from the open field experiment on 14 Sep 2016 and up to 300 m for the forested experiment on 15 Sep 2016, as depicted in Fig. 14. The relevant atmospheric conditions for these two days are summarized in Table 2.

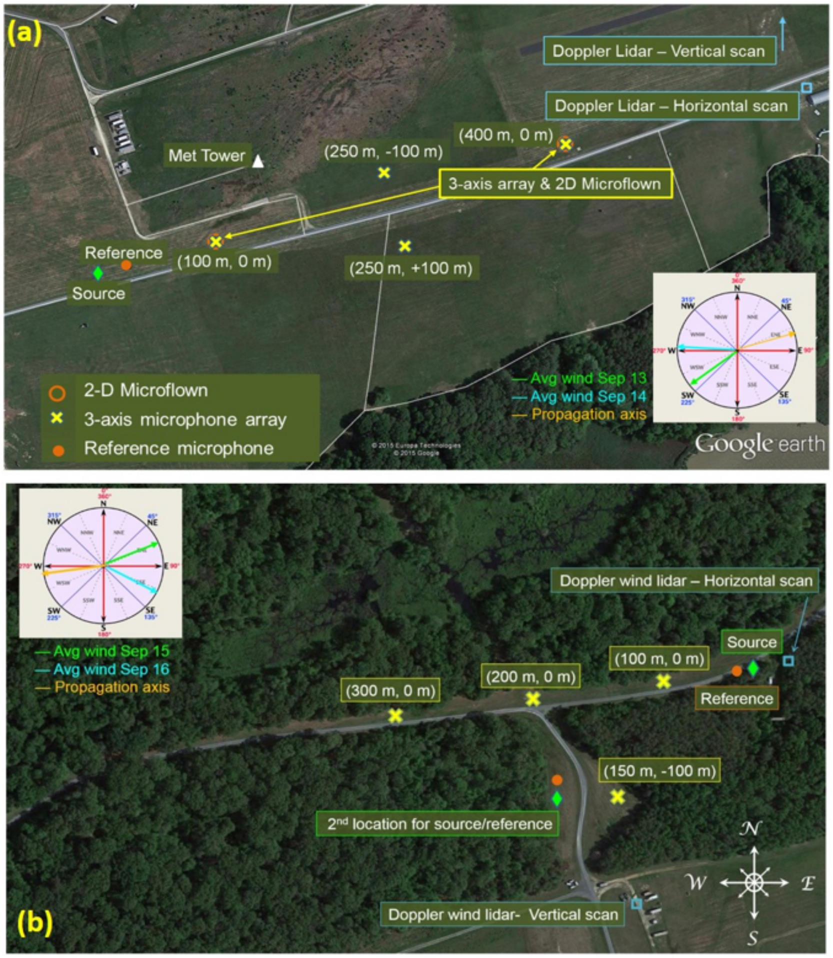

Fig. 14 Experimental setup: a) open field 13–14 Sep 2016 and b) forested area 15–16 Sep 2016 (images: Google Earth)

Table 2 Varying source distribution: correlation coefficient median and IQR statistics for MDD and CC Green's function retrieval: δ propane cannon, S_1 foghorn, and S_4 broadband. CC only given for the propane cannon.

Date	Source-to-center radius	No. of sources	Source	Median ρ MDD (CC)	IQR ρ MDD (CC)
14 Sep 2016	250 m	1	δ	0.73 (0.71)	0.06 (0.06)
14 Sep 2016	250 m	1	S_4	0.50	0.06
1 Sep 2017	300 m	1	δ	0.85 (0.87)	0.01 (0.01)
30 Aug 2017	500 m	1	δ	0.80 (0.88)	0.03 (0.01)
30 Aug 2017	500 m	1	S_1	0.70	0.01
30 Aug 2017	500 m	1	S_4	0.77	0.01
1 Sep 2017	300 m	5	δ	0.43 (0.48)	0.03 (0.02)
1 Sep 2017	300 m	5	S_1	0.55	0.06
1 Sep 2017	300 m	5	S_4	0.24	0.19

A propane cannon was used to generate an impulsive source, $S(t;\mathbf{r}_0) \approx \delta(t)$, every 20 s. The nonimpulsive, broadband, audible controlled sources were played through loudspeakers. The broadcast sources we consider here are S_1 a recorded foghorn, S_2 a synthesized “twirl”, and S_3 a synthesized “decompression”. The recorded measured responses (pressure fields) were filtered with an eighth-order zero-phase Butterworth bandpass filter with a lower 3-dB cutoff frequency of 60 Hz and an upper 3-dB cutoff frequency of 3 kHz. Thereafter, a Weiner filter was applied to the recorded data. Figure 15 shows typical normalized pressure signals in the open field at the 10-m reference microphone in the upper plots and the corresponding power spectral density in the lower plots for the propane cannon and these three broadcast signals.

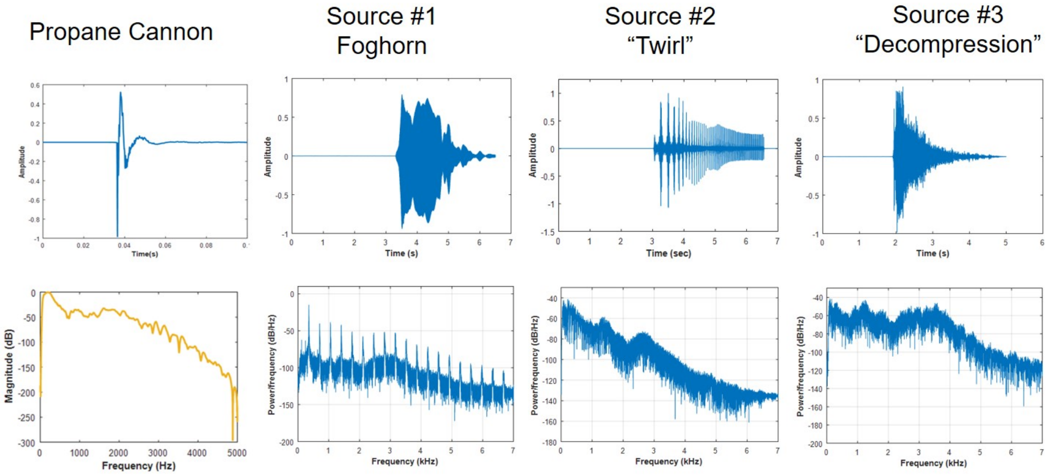
Propane Cannon

Source #1
Foghorn

Source #2
“Twirl”

Source #3
“Decompression”

Fig. 15 Typical received signals (normalized) measured in the open field at the 10-m reference microphone (top row) and corresponding power spectral density (bottom row)

For each considered case, the retrieved Green’s function $\hat{G}(\mathbf{r}_l^B, \mathbf{r}_\nu^A, t)$ between element ν of array A (located at $\mathbf{r}_\nu^A$) and element l of array B (located at $\mathbf{r}_l^B$) is obtained between all elements of the two arrays, $(\nu, l) = [1, \ldots, N = 12]$. When all 12 microphones on each array are properly functioning, this corresponds to 144 retrievals.

For the open field experiment, let us consider the arrays that are separated by 300 m on the propagation axis: array A, whose center is located at $x_c^A = 100$ m downrange of the source, and array B, whose center is located at $x_c^B = 400$ m downrange. In the forested area, let us consider the arrays with an on-axis separation of 200 m, corresponding to the array centers located at $x_c^A = 100\,\mathrm{m}$ and $x_c^B = 300\,\mathrm{m}$ downrange.

Figure 16 shows typical spectrograms for pressure field measurements of three propane cannon shots in the open field: the unfiltered signal measured at the 10-m reference microphone (upper left), and the filtered signal measured at the reference microphone (lower left), 100-m array (upper right), and 400-m array (lower right). Physically, the signal is decaying as it propagates forward and this decay is frequency-dependent—spherical spreading, ground absorption, and atmospheric absorption all play a role. The propane cannon has a large absolute amplitude; therefore, while we observe a reduced SNR at 400 m with respect to that at 100 m, the SNR is still high. We also notice some interfering noise sources at 100 m (after 40 s), that are slightly more pronounced at the 400-m array. Similar results are seen for the forested area.

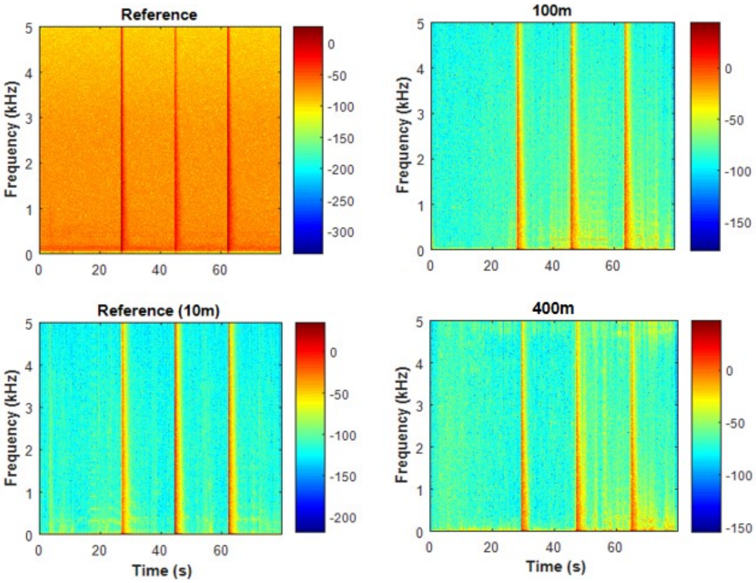

Fig. 16 Spectrogram of propane cannon measured in the open field: (upper left) unfiltered and (lower left) filtered reference signals; (upper right) 100-m array and (lower right) 400-m array filtered signals

The corresponding retrieved Green's functions for both the CC and MDD methods are shown in Fig. 17 as a function of time a) in the open field and b) in the forested area. For brevity in presentation, only the results across like channels, $\nu = l$ (vertical label) are shown. It should be noted that some technical difficulties were encountered acquiring data in microphone array element $\nu = 7$ throughout the experiment; therefore, our analyses exclude the data from channel 7 on both arrays. Comparison of the two retrieval methods finds that approximating the autocorrelation function of the propane cannon as a delta function is a reasonable assumption for the CC method.

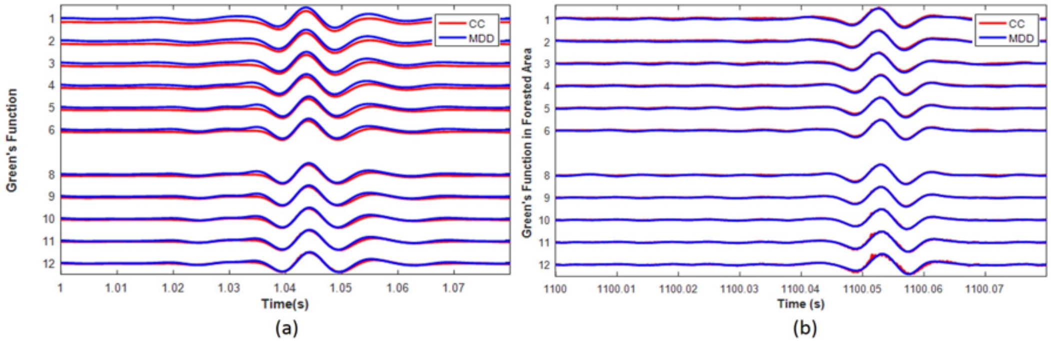

Fig. 17 Retrieved Green's functions for a propane cannon in the a) open field and b) forested area between like elements ($\nu = l$) of arrays A and B. CC method is red and MDD is blue

Similarly, the spectrograms for the foghorn S_1, twirl S_2, and decompression S_3 are given in Fig. 18 for the open field. These sources were broadcast through loudspeakers and had a much lower source amplitude than the propane cannon. The decompression sound, S_3, had the lowest amplitude of these signals. This is evident in the spectrograms. The SNR is reduced at 100 m compared to the reference microphone measurements at 10 m. At 400 m, the SNR is notably reduced for all signals. For S_3, there is significant loss of signal content after 30 s. Examples of the retrieved CC and MDD Green's functions are shown in Fig. 19, again for $A = 100\,\mathrm{m}$ and $B = 400\,\mathrm{m}$. Since the autocorrelation function of these sources does not approach a delta function, the retrieved CC represents the retrieved medium response function and not the impulse response function. For this specific case, the MDD retrieval of the Green's function for S_3 failed. Low signal to noise can lead to instabilities in the inversion (i.e., varying the value of ϵ in Eq. 32 did not result in a stable inversion).

S_1: Foghorn, Open Field

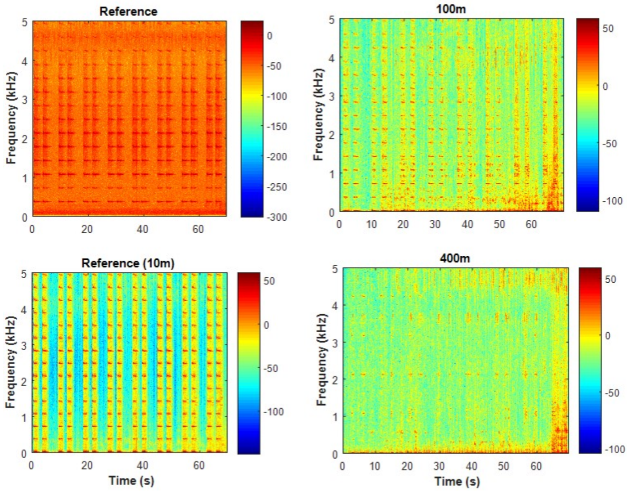

S_2: Twirl, Open Field

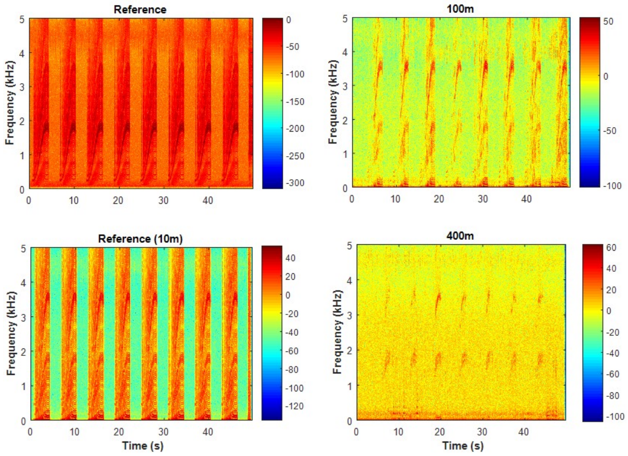

S_3: Decompression, Open Field

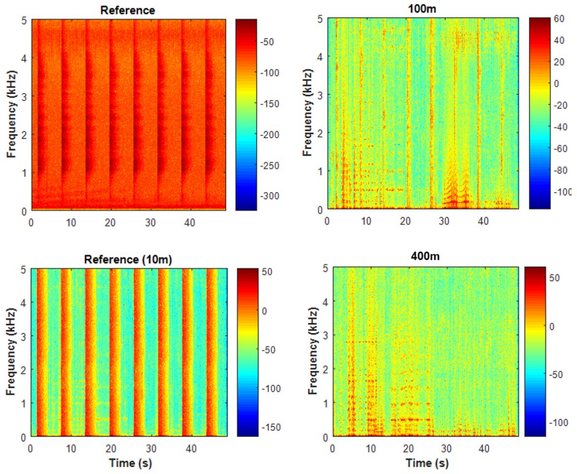

Fig. 18 Spectrograms for nonimpulsive source S_1, S_2, and S_3 measured in the open field. For each source: (upper left) unfiltered and (lower left) filtered reference signals; (upper right) 100-m array and (lower right) 400-m array filtered signals

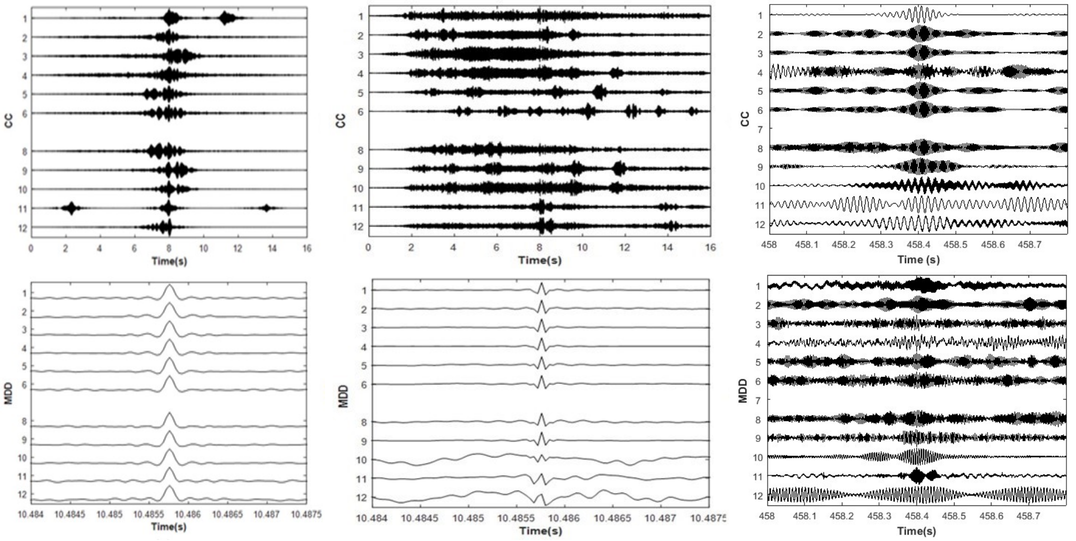

Fig. 19 CC (upper) and MDD Green's function (lower) retrievals for nonimpulsive sources (left) foghorn S_1, (center) twirl S_2, and (right) decompression S_3 between arrays $A = 100\,\mathrm{m}$ and $B = 400\,\mathrm{m}$ in the open field

The spectrograms for measurements of sources S_1, S_2, and S_3 in the forest are shown in Fig. 20. Again there is a notable reduction in SNR at the furthest array, located 300 m downrange. The retrieved MDD Green's function between arrays $A = 100\,\mathrm{m}$ and $B = 300\,\mathrm{m}$ is shown in Fig. 21. For this case the retrieval for S_3 did not fail, though we do see small oscillations outside the signal window—again this is most probably due to the numerical inversion.

S_1: Foghorn, Forest

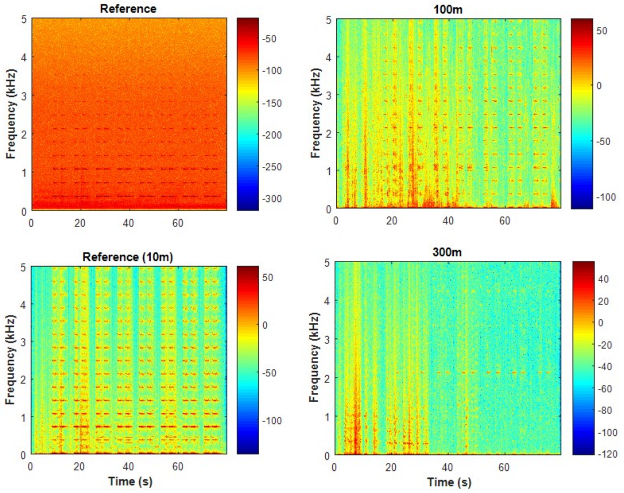

S_2: Twirl, Forest

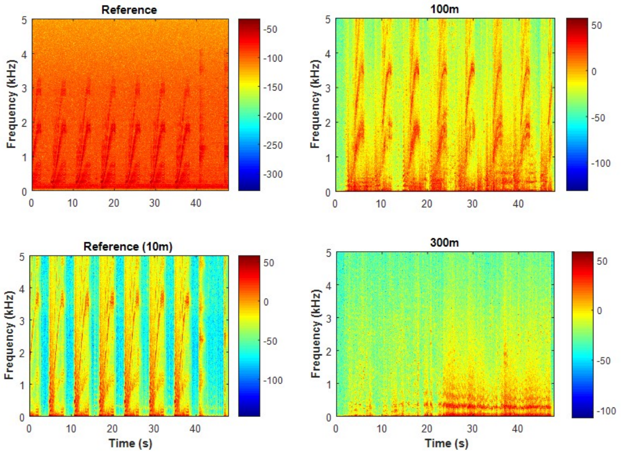

S_3: Decompression, Forest

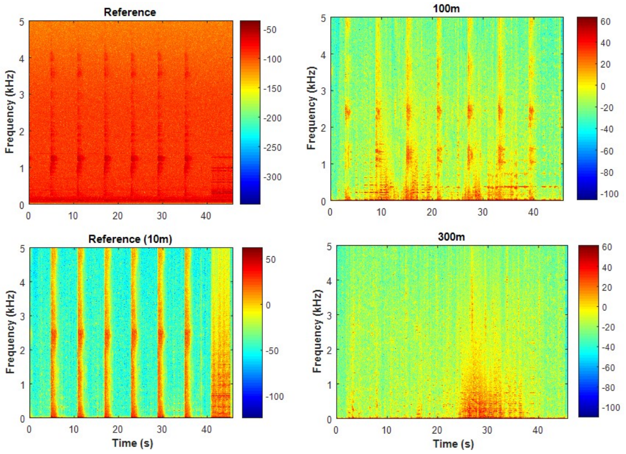

Fig. 20 Spectrograms for nonimpulsive source S_1, S_2, and S_3 measured in the forest. For each source: (upper left) unfiltered and (lower left) filtered reference signals; (upper right) 100-m array and (lower right) 300-m array filtered signals.

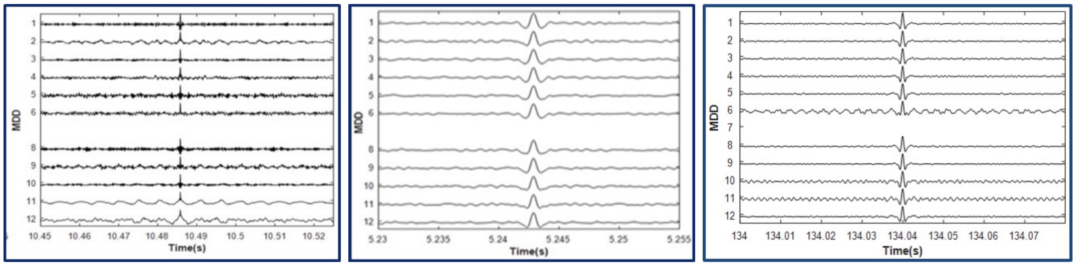

Fig. 21 MDD Green's function retrievals for nonimpulsive sources (left) foghorn S_1, (center) twirl S_2, and (right) decompression S_3 measured in the forest between arrays $A = 100\,\mathrm{m}$ and $B = 300\,\mathrm{m}$

Let us now consider an application. The Green's function is retrieved from the impulsive events (propane cannon shots) between the 100-m array (A) and the 400-m array (B), then applied to predict the received signal at the 400-m array using the recorded signal at the 100-m array. That is, we are comparing the measured response $p_\delta(\mathbf{r}_l^B, t)$ to the predicted response $p_\delta(\mathbf{r}_\nu^A, t) * \hat{G}_\delta^{\mathrm{CC,MDD}}(\mathbf{r}_l^B, \mathbf{r}_\nu^A; t)$. For one pulse, there are 121 retrievals used in the analysis (corresponding to all combinations of the microphone elements $l, \nu = [1, \ldots, 6, 8, \ldots, 12]$ across the two arrays). Figure 22 compares the measured signal (blue) for the propane cannon to the predicted signal (red) for open field propagation. The cases shown correspond to the maximum correlation coefficient of $\rho_{\mathrm{max},\delta}^{\mathrm{CC}} = 0.92$ for the CC method, and $\rho_{\mathrm{max},\delta}^{\mathrm{MDD}} = 0.97$ for the MDD method. The box plots for the correlation coefficients across the 121 retrievals are also presented. The median correlation coefficient for the CC method is $\bar{\rho}_\delta^{\mathrm{CC}} = 0.70$ with an interquartile range of $\mathrm{IQR}_\delta^{\mathrm{CC}} = 0.87$, and for the MDD method $\bar{\rho}_\delta^{\mathrm{MDD}} = 0.75$ and $\mathrm{IQR}_\delta^{\mathrm{MDD}} = 0.93$.

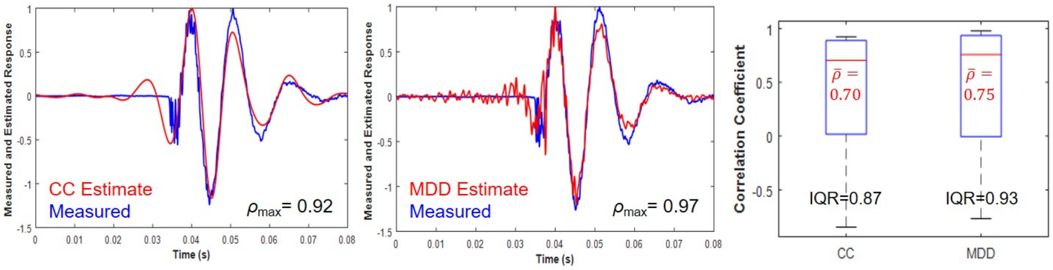

Fig. 22 Estimated response $p_\delta(\mathbf{r}_\nu^A, t) * \hat{G}_\delta^{\mathrm{CC,MDD}}(\mathbf{r}_l^B, \mathbf{r}_\nu^A; t)$ compared with measured response $p_\delta(\mathbf{r}_l^B, t)$ for a propane cannon detected at $A = 100\,\mathrm{m}$ and $B = 400\,\mathrm{m}$ in the open field

Similarly for the forested area, Fig. 23 compares the measured response to a propane cannon shot $p_\delta(\mathbf{r}_l^B, t)$ to the predicted response $p_\delta(\mathbf{r}_\nu^A, t) * \hat{G}_\delta^{\mathrm{CC,MDD}}(\mathbf{r}_l^B, \mathbf{r}_\nu^A; t)$ for $A = 100\,\mathrm{m}$ and $B = 300\,\mathrm{m}$. Again, the cases with the maximum correlation coefficient are presented: $\rho_{\max,\delta}^{\mathrm{CC,MDD}} = 0.81$ for both CC and MDD methods. The box plots across the 121 retrievals are also shown, with $\bar{\rho}_\delta^{\mathrm{CC}} = 0.28$ and $\mathrm{IQR}_\delta^{\mathrm{CC}} = 0.94$ for the CC method, and $\bar{\rho}_\delta^{\mathrm{MDD}} = 0.29$ and $\mathrm{IQR}_\delta^{\mathrm{MDD}} = 0.72$ for the MDD method.

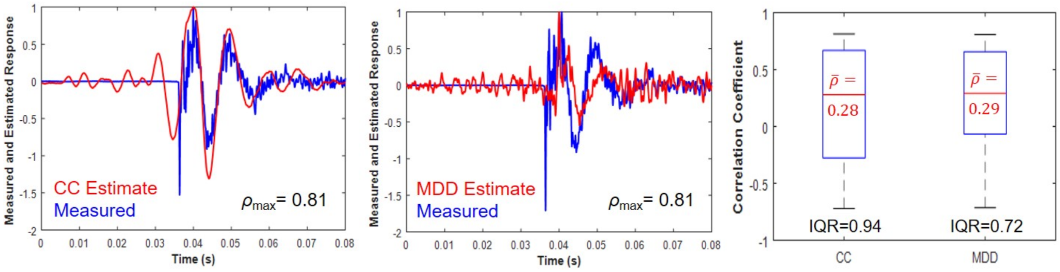

Fig. 23 Estimated response $p_\delta(\mathbf{r}_\nu^A, t) * \hat{G}_\delta^{\mathrm{CC,MDD}}(\mathbf{r}_l^B, \mathbf{r}_\nu^A; t)$ compared with measured response $p_\delta(\mathbf{r}_l^B, t)$ for a propane cannon detected at $A = 100\,\mathrm{m}$ and $B = 300\,\mathrm{m}$ in the forested area

Using the MDD-retrieved Green's functions for the nonimpulsive sources S_1, S_2, and S_3 (not pictured), we find that the maximum correlation coefficients are less than 0.5 when comparing the estimated versus measured responses.

7. Green's Function Retrieval: Propagation Distances > 400 m

In this section, we consider Green's function retrieval for propagation distances up to 600 m in an open field. The experimental configuration is shown in Fig. 24. We consider data collected on 30 Aug 2017.

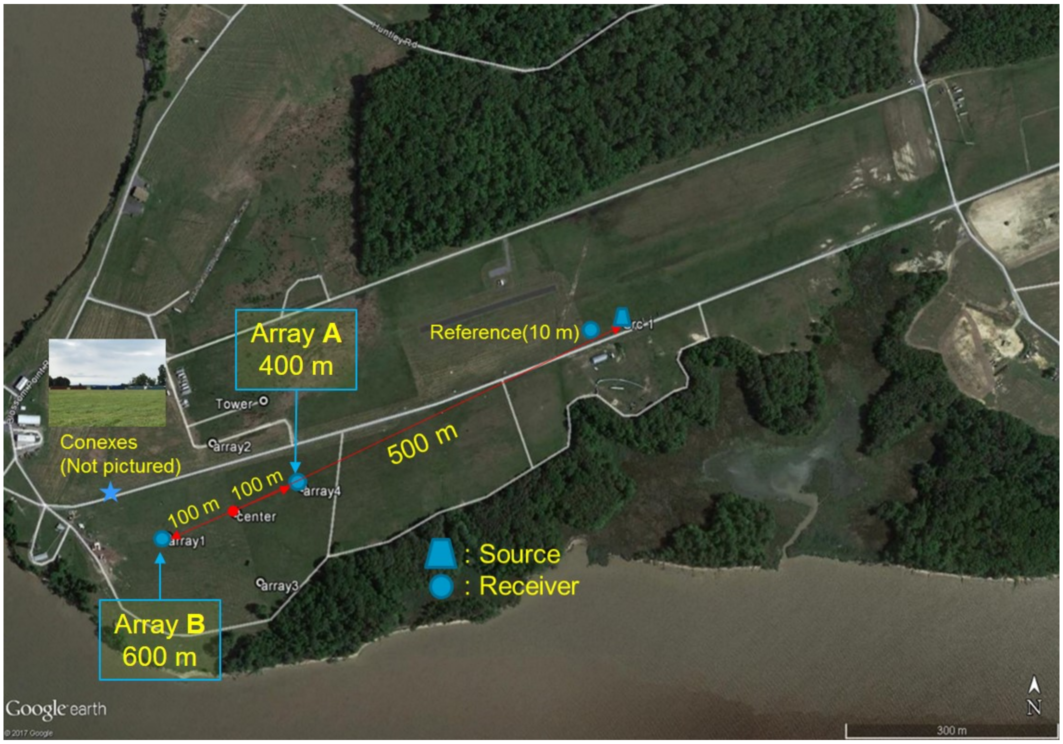

Fig. 24 Experimental setup for long-range propagation tests (image: Google Earth)

Examples of the CC and MDD retrieved Green's functions between $A = 400\,\mathrm{m}$ and $B = 600\,\mathrm{m}$ arrays (on the propagation axis) for a propane cannon shot are shown in Fig. 25. For this experiment, all 12 microphones are considered, leading to 144 retrievals per event. Therefore, for brevity, Fig. 25 only shows retrievals across like elements of the two arrays (vertical label), $g_\delta^{\mathrm{CC}}(\mathbf{r}_l^B, \mathbf{r}_l^A; t)$ (left) and $g_\delta^{\mathrm{MDD}}(\mathbf{r}_l^B, \mathbf{r}_l^A; t)$ (right).

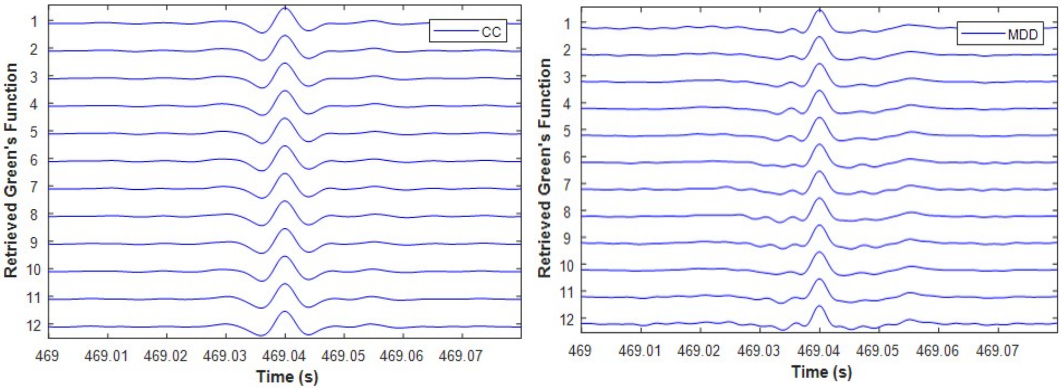

Fig. 25 Long-range propagation Green's function retrieval using propane cannon: (left) CC and (right) MDD

The measured responses at B, $p_\delta(\mathbf{r}_l^B, t)$, are then compared to the predicted responses at B, $p_\delta(\mathbf{r}_\nu^A, t) * \hat{G}_\delta^{\text{CC,MDD}}(\mathbf{r}_l^B, \mathbf{r}_\nu^A; t)$, for all 144 cases. Figure 26 depicts the cases with the maximum correlation coefficients: $\rho_{\max,\delta}^{\text{CC}} = 0.92$ for the CC method and $\rho_{\max,\delta}^{\text{MDD}} = 0.96$ for the MDD method. The corresponding box plots across the 144 retrievals are also shown. The CC and MDD methods have a median correlation coefficient of $\bar{\rho}_\delta^{\text{CC,MDD}} = 0.77$, with interquartile values of $\text{IQR}_\delta^{\text{CC}} = 1.07$ and $\text{IQR}_\delta^{\text{MDD}} = 0.77$.

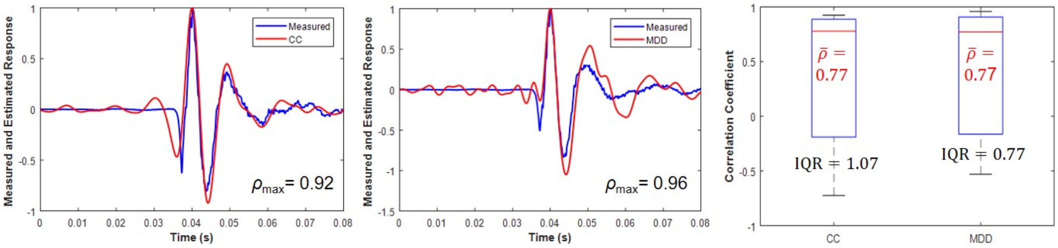

Fig. 26 Long-range propagation estimated response $p_\delta(\mathbf{r}_\nu^A, t) * \hat{G}_\delta^{\text{CC,MDD}}(\mathbf{r}_l^B, \mathbf{r}_\nu^A; t)$ compared with measured response $p_\delta(\mathbf{r}_l^B, t)$ for a propane cannon shot detected at $A = 400\,\text{m}$ and $B = 600\,\text{m}$

Figure 27 shows example MDD Green's function retrievals for the nonimpulsive sources S_1, S_2, and S_3. We notice oscillations, particularly from S_1 and S_3. While this may be due to numerical instabilities in the inversion or low SNR, it may also be that the MDD method is not fully removing the source function. These results are then used to compare the measured response $p_{S_i}(\mathbf{r}_l^B, t)$ to the estimated response $p_{S_i}(\mathbf{r}_\nu^A, t) * G_{S_i}^{\text{MDD}}(\mathbf{r}_l^B, \mathbf{r}_\nu^A; t)$ for each S_i. Figure 28 show the results for the maximum correlation coefficients, as well as the box plots for the correlation coefficients and SNRs. An interesting note in these comparisons is the good phase alignment, particularly for S_3.

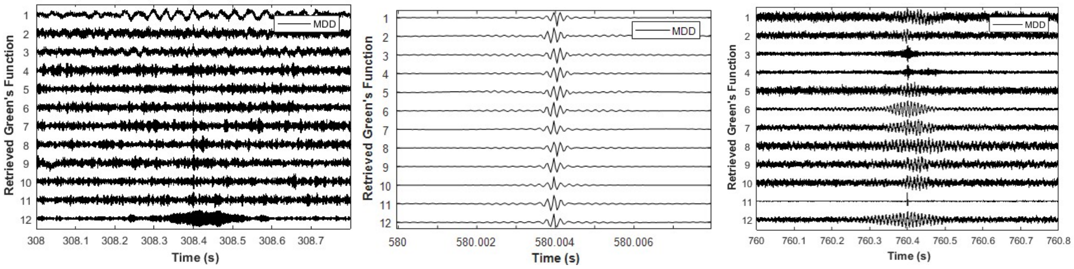

Fig. 27 Long-range propagation MDD Green's function retrieval for nonimpulsive sources S_1, S_2, and S_3

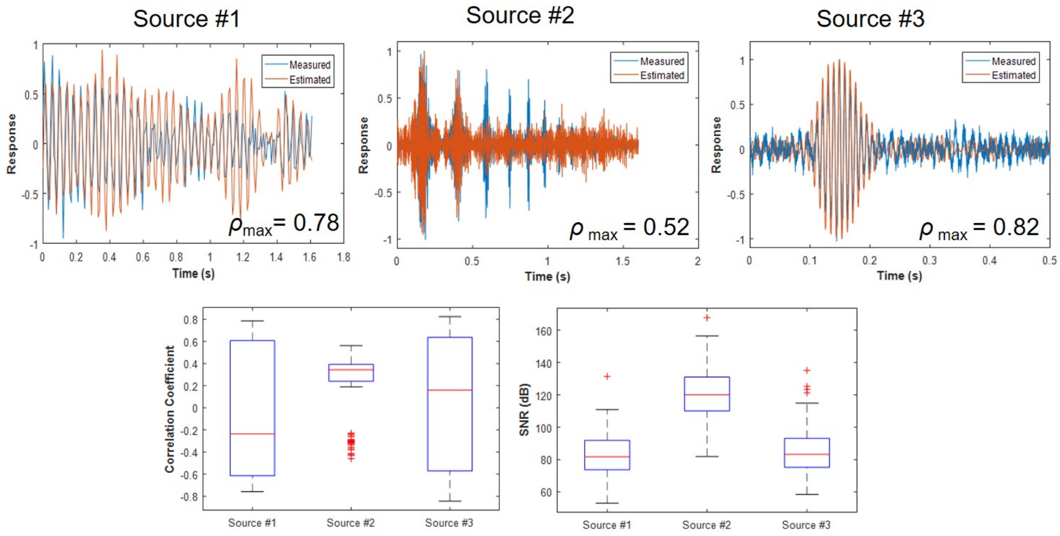

Fig. 28 Long-range propagation estimated response $p_{S_i}(\mathbf{r}_l^A, t) * G_{S_i}^{\mathrm{MDD}}(\mathbf{r}_l^B, \mathbf{r}_l^A; t)$ compared with measured response $p_{S_i}(\mathbf{r}_l^B, t)$ for nonimpulsive sources S_1, S_2, and S_3 detected at $A = 400\,\mathrm{m}$ and $B = 600\,\mathrm{m}$

8. Green's Function Retrieval: Influence of Source Distribution

Additional experiments were conducted allowing examination of the effect of the source distribution. The distance between the source and the center of the array stations we term the source-to-array center radius. Figure 29a–c shows the three experimental setups we consider to compare the retrieved Green's function for three different source-to-array center radii, $r_{\odot}$: a) 500 m, b) 300 m, and c) 250 m. Only a single source is considered. Figure 29d shows the experimental setup used to investigate the effect of the angular distribution of sources on Green's function retrieval: five sources are uniformly distributed along a circular arc of radius 300 m from the array center in 38° increments. For the propane cannon, the shots were done sequentially from each source location (only a single propane cannon was used, and thus had to be moved for each source location). For the nonimpulsive broadcast signals, a loud speaker was located at each source location and all five speakers broadcast simultaneously. It should also be noted that for b) and d), the arrays were no longer aligned with the propagation axis. The array element numbering and axis alignment with respect to north remains as for a), since the arrays were left in place and the sources moved.

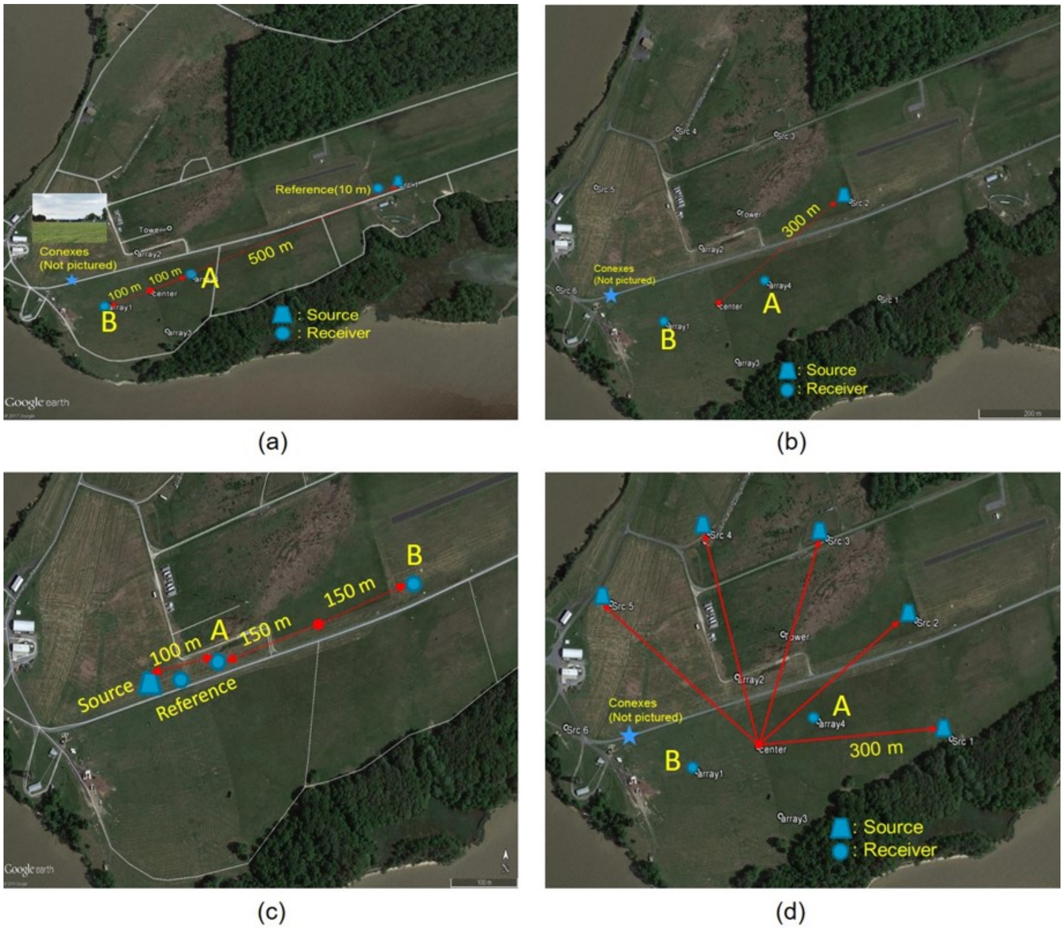

(a)

(b)

(c)

(d)

Fig. 29 Experimental setups with varying source-to-array center radii (images: Google Earth)

For the analyses in this section, we consider a propane cannon and two nonimpulsive broadband sources, as shown in Fig. 30. The first nonimpulsive source is the foghorn S_1, and the other wideband source S_4 has a ramp up in amplitude followed by a decay.

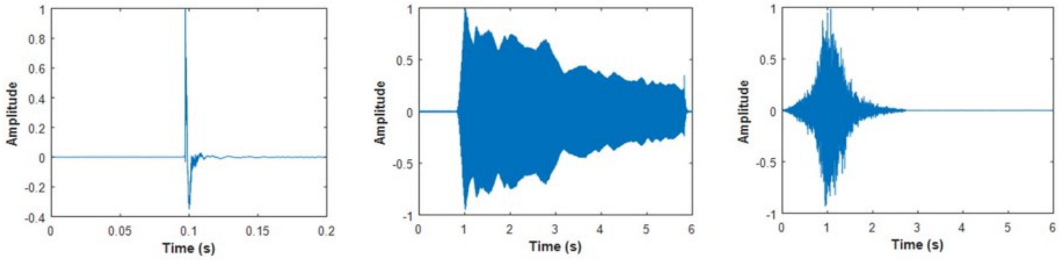

(a) (b) (c)

Fig. 30 Normalized pressure responses for sources considered in the source distribution study: a) propane cannon, b) foghorn S_1, and c) broadband source S_4

First let us consider the effect of varying the source-to-array center radius. Figure 31 shows examples of the retrieved Green's function for the experiment shown in Fig. 29a (long range), $r_\odot = 500\,\mathrm{m}$. Figure 31a compares the retrieved Green's function using the CC and MDD methods for the propane cannon and the the MDD method for S_1. Similarly, Fig. 31b shows example comparisons for S_4. We see good agreement for all cases. As before, we now use the retrieved Green's functions to estimate the response. Figure 31c compares the measured response $p_\delta(\mathbf{r}_l^B, t)$ to the estimated response $p_\delta(\mathbf{r}_\nu^A, t) * \hat{G}_\delta^{\mathrm{CC}}(\mathbf{r}_l^B, \mathbf{r}_\nu^A; t)$ using the CC retrieval for the propane cannon; Fig. 31d similarly compares for the MDD retrieval for the propane cannon. The cases depicted correspond to the maximum achieved correlation coefficients, which is greater than 0.9 for both the CC and MDD methods.

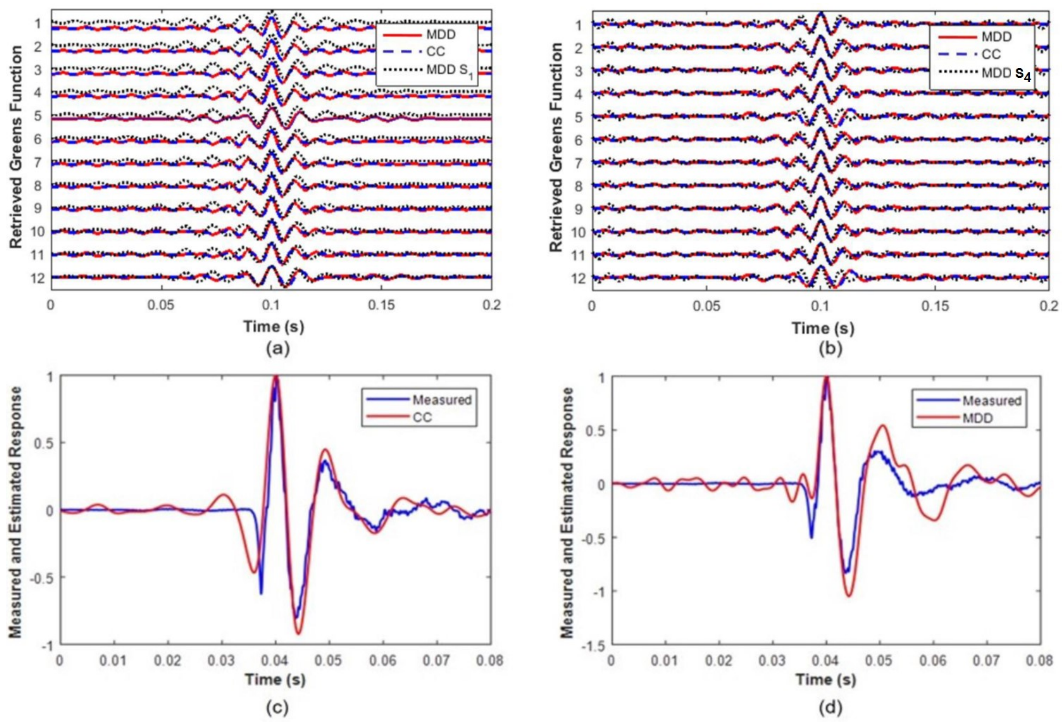

Fig. 31 Retrieved Green's function for $r_\odot = 500\,\mathrm{m}$ for the source waveforms: a) MDD and CC propane cannon Green's function, and the MDD recorded signal S_1 Green's function, and b) MDD and CC propane cannon Green's function, and the MDD recorded signal S_4 Green's function. Estimated response $p_\delta(\mathbf{r}_\nu^A, t) * \hat{G}_\delta(\mathbf{r}_l^B, \mathbf{r}_\nu^A; t)$ (red) and measured response $p_\delta(\mathbf{r}_l^B; t)$ (blue) for the propane cannon using the c) CC and d) MDD methods for the maximum correlation coefficient cases, $\rho_{\max,\delta}^{\mathrm{CC}} = 0.92$ and $\rho_{\max,\delta}^{\mathrm{MDD}} = 0.96$, respectively.

The statistical comparisons of the correlation coefficient for all the experimental setups using the CC and MDD retrieved Green's function are summarized in Table 2. High median correlation coefficient values ($\rho > 0.7$) were observed for the 250-, 300-, and 500-m source-to-array center radii single-source experiments, except for S_4 with $r_\odot = 250\,\mathrm{m}$ ($\rho = 0.5$). Also, low IQR values ($\rho < 0.1$) were observed in all the single-source experiments, signifying that most of the correlation coefficient values were close to the median. Additionally, the median correlation coefficient for the $r_\odot = 250\,\mathrm{m}$ experiment is less than those for the 300- and 500-m single-source experiments. Note, the station-to-station distance in the former case is larger (300 m) in comparison to the latter cases (200 m).

Comparisons between single- and multiple-source experiments in Table 2 demonstrate that adding more sources in Fig. 29d lowers the median correlation coefficients ($\bar{\rho} < 0.55$) for experiments with the same array station-to-station distance

(200 m) for 300- and 500-m source-to-array center radii. The lower correlation coefficients for the prerecorded sounds maybe attributed to the different propagation paths from each source (due to the angular distribution) relative to each array station, as opposed to the complications of the source waveform. This may be supported by the results of the propane cannon, which display low median correlation coefficients ($\bar{\rho} < 0.5$) for both the MDD and CC methods. Therefore, a different configuration other than uniform angular distribution may need to be considered for the retrieval of the Green's function for the scenario of multiple controlled sources in a nondiffused field.

Additionally, the assumptions on the propagation environment may contribute. While the wind speeds were low, ≤ 3.0 m/s for 30 Aug and 1 Sep 2017, there was more variability in wind direction. Moving the propane cannon to each of the five source locations means that the environmental state may have changed sufficiently to be observed in the statistical analysis. The relative orientation between the sources and receivers could also contribute.

9. Conclusions

In summary, we have examined two methods of retrieving the Green's function for outdoor sound propagation using audible sources with a limited number of receiving arrays: CC and MDD. The CC method is only valid when the autocorrelation function of the source approaches a delta function, for example, propane cannon shots. The MDD method removes the PSF, and thus in theory, can be applied to other broadband sources. The good agreement between the CC and MDD methods for the propane cannon validates the assumption that the autocorrelation function for the propane cannon may be approximated as a delta function.

The analysis presented here assumes that the propagation medium is constrained: approximate spatial reciprocity, approximate time invariance over the analysis window, and sufficient statistics to capture the random medium. Additionally, it was shown that for low flow velocity (Mach numbers below 0.15) that flow reversal need not be considered. We have considered propagation distances up to 600 m.

As a measure of performance of the retrieval, we compared measured pressure field responses to predicted pressure field responses using the retrieved Green's function, calculating the statistics of the corresponding correlation coefficient. When considering single sources, the propane cannon yielded the highest correlation coefficients in the open field, with median values exceeding 0.7 and maximum values exceeding 0.9. The forested area had lower correlation coefficients for both the CC and MDD methods, with median values less than 0.3 and IQRs greater than 0.7. For the nonimpulsive broadband sources examined, we found that the maximum correlation coefficient exceeded 0.5. When considering multiple sources with a uniform angular distribution about the array stations center, the correlation coefficients were found to be less than 0.5.

The results suggest that source-to-receiver distance does not degrade the accuracy of the Green's function retrieval, except when the source-to-array center distance is large in comparison to the station-to-station array distance. Fan and Snieder[43] analytically demonstrated that the source-to-array center distance has negligible effects on Green's function retrieval, but only when the source-to-array center radius is much larger than the distance between the two receivers. The influence of increasing the number of sources requires further investigation.

Overall, MDD Green's function retrieval has better performance based on correlation coefficient and other statistical measures, and reduces the constraints on the source. Use of MDD for broadband source results in better signal reconstruction, particularly, phase alignment, when considering the same source. Further investigation is required to determine whether the MDD sufficiently removes the source autocorrelation function under a variety of propagation environments. Moreover, the cases considered were for low flow velocity. Additional analyses are needed for other environmental states.

This research is continuing to mission, where applications such as acoustic tomography of the atmosphere and beamforming are being considered.

10. Metrics

The results of this research project have been published/presented as follows:

1. Denis MF, Collier SL, Noble JM, Alberts II WCK, Ligon DA, Sim LK, Reiff CG, James DD. Outdoor acoustic tomography using retrieved Green's function from controlled-sources: an experimental feasibility study. 175th Meeting of the Acoustical Society of America; 2018 May 7–11. J Acoust Soc Am.

2018;143:1722.

2. Denis MF, Collier SL, Noble JM, Alberts II WCK, Ligon DA, Sim LK, Reiff CG, James, DD. Performance of Green's function retrieval methods for various sound source distributions: application to outdoor acoustic propagation. 174th Meeting of the Acoustical Society of America; 2017 Dec 4–8; New Orleans, LA. J Acoust Soc Am. 2017;142:2674.
3. Denis MF, Collier SL, Ligon DA, Noble JM, Alberts II WCK, Sim LK, Reiff CG, James DD. Comparison of Green's function retrieval methods for outdoor sound propagation. Proceedings of the 2017 Meeting of the Military Sensing Symposia (MSS) Specialty Group On Battlespace Acoustic, Seismic, Magnetic, and Electric-Field Sensing and Signatures (BAMS); 2017 Oct 31–Nov 2; Springfield, VA.
4. Denis MF, Collier SL, Noble JM, Alberts II WCK, Ligon DA, Sim LK, Reiff CG, James DD. Green's function retrieval by cross correlation and multidimensional deconvolution: application to atmospheric acoustics. Acoustics 2017; 25–29 Jun 2017; Boston, MA. J Acoust Soc Am. 2017;141:3885.
5. Collier SL, Ligon DA, Cain JE, Noble JM, Alberts II WCK, Sim LK, James DD, Reiff CG. Green's function retrieval for outdoor sound propagation. Proceedings of the International Symposium on Long Range Sound Propagation; 2016 Sep 20–21; Oxford, MS.
6. Collier SL, Ligon DA, Cain JE, Noble JM, Alberts II WCK, Sim LK. Green's function estimation for outdoor sound propagation. Proceedings of the Joint Meeting of the Military Sensing Symposium; 2016 June 20–23; Gaithersburg, MD.
7. Collier SL, Ligon DA, Cain JE, Noble JM, Alberts II WCK, Sim LK. Inverse methods for Green's function retrieval. 171st Meeting of the Acoustical Society of America (invited); 2016 May 23–27; Salt Lake City, UT. J Acoust Soc Am. 2016;139:1985.
8. Collier SL, Cain JE, Noble JM, Alberts II WCK, Ligon DA, Sim LK. Green's function retrieval for atmospheric acoustic propagation. 170th Meeting of the Acoustical Society of America (invited); 2015 Nov 2–6; Jacksonville, FL. J Acoust Soc Am. 2015;138:1754.

11. References

1. Ostashev VE, Wilson DK, Collier SL, Cain JE, Cheinet S. Cross-frequency coherence and pulse propagation in a turbulent atmosphere. J Acoust Soc Am. 2016;140:678–691.

2. Cheinet S, Cosnefroy M, Wilson D, Ostashev V, Collier S, Cain J. Effets de la turbulence sur des impulsions acoustiques se propageant prés du sol. Proc CFA/VISHNO 2016; 2016 Apr 11–14; Le Mans, France. 45–51. http://www.conforg.fr/cfa2016/cdrom/data/articles/000159.pdf.

3. Ostashev VE, Wilson DK, Vecherin SN, Collier SL. Spatial-temporal coherence of acoustic signals propagating in a refractive turbulent atmosphere. J Acoust Soc Am. 2014;136:2414–2431.

4. Cain JE, Collier SL, Ostashev VE, Wilson DK. Statistical moments of a wideband acoustic signal. Proc Mtgs Acoust. 2014;21:045004.

5. Candy JV, Meyer AW, Poggio AJ, Guidry B. Time-reversal processing for an acoustic communications experiment in a highly reverberant environment. J Acoust Soc Am. 2004;115:1621–1631.

6. Candy JV, Poggio AJ, Chambers DH, Guidry BL, Robbins CL, Kent CA. Multichannel time-reversal processing for acoustic communications in a highly reverberant environment. J Acoust Soc Am. 2005;118:2239–2354.

7. Candy JV, Chambers DH, Robbins CL, Guidry BL, Poggio AJ, Dowla F, Hertzog CA. Wideband multichannel time-reversal processing for acoustic communications in highly reverberant environments. J Acoust Soc Am. 2006;120:838–851.

8. Wapenaar K. Nonreciprocal Green's function retrieval by cross correlation. J Acoust Soc Am. 2006;120:EL7–EL13.

9. Wapenaar K. Retrieving the elastodynamic Green's function of an arbitrary inhomogeneous medium by cross correlation. Phys Rev Lett. 2004;93:254301.

10. Carminati R, Pierrat R, de Rosny J, Fink M. Theory of the time reversal cavity for electromagnetic fields. Optics Letters. 2007;32:3107–3109.

11. Derode A, Larose E, Tanter M, de Rosny J, Tourin A, Campillo M, Fink M Recovering the Green's function from field-field correlations in an open scattering medium. J Acoust Soc Am. 2003;113:2973–2976.

12. Fink M. Time-reversed acoustics. Phys Today. 1997;40:34–40.

13. Fink M. Time reversal of ultrasonic fields, part I: basic principles. IEEE Trans on Ultrasonics, Ferroelectrics, and Frequency Control. 1992;39:555–566.

14. Kuperman WA, Hodgkiss WS, Song HC, Akal T, Ferla C, Jackson DR. Phase conjugation in the ocean: experimental demonstration of an acoustic time-reversal mirror. J Acoust Soc Am. 1998;103:25–40.

15. Marengo EA, Gruber FK. Optical-theorem-based coherent scatterer detection in complex environments. International Journal of Antennas and Propagation. 2013;231729.

16. Moura JMF, Jin Y. Detection by time reversal: single antenna. IEEE Trans Sig Proc. 2007;55:187–201.

17. Ni S. Preface to the special issue on earthquake geodesy. Earthq Sci. 2011;24:133-134.

18. Sabra KG, Gerstoft P, Roux P. Extracting time-domain Green's function from ambient seismic noise. Geophys Res Lett. 2005;32:L03310.

19. Slob E, Draganov D, Wapenaar K. In: Proc. of the 11th International Conference on Ground Penetrating Radar; 2006.

20. Snieder R. Extracting the Green's function of attenuating heterogeneous acoustic media from uncorrelated waves. CWP-556. 2006:147–154.

21. Snieder R, Slob E, Wapenaar K. Lagrangian Green's function extraction, with applications to potential fields, diffusion and acoustic waves. New Journal of Physics. 2010;12:063013.

22. Sutin A, Johnson P, TenCate J, Sarvazyan A. Time reversal acousto-seismic method for land mine detection. Proc of SPIE. 2005;5794:708–716.

23. Sutin A, Libbey B, Kurtenoks V, Fenneman D, Sarvazyan A. Nonlinear detection of land mines using wide band width time-reversal techniques. Proc of SPIE. 2006;6217:62171B-1–12.

24. Thomas J-L, Wu F, Fink M. Time reversal mirror applied to lithotripsy. Ultrason Imaging. 1996;18:106–21.

25. Weaver RL, Lobkis OI. Diffuse fields in open systems and the emergence of the Green's function. J Acoust Soc Am. 2004;116:2731–2734.

26. Weaver RL, Lobkis OI. Diffuse fields in ultrasonics and seismology. Geophysics. 2006;71:SI5–SI9.

27. Xu Y, Wang LV. Time reversal and its application to tomography with diffracting sources. Phys Rev Lett. 2004;92(033902):1–4.

28. Yang TC, Yang W-B. Low probability of detection underwater acoustic communications using direct-sequence spread spectrum. J Acoust Soc Am. 2008;124:3632–3647.

29. Yon S, Tanter M, Fink M. Sound focusing in rooms: the time-reversal approach. J Acoust Soc Am. 2003;113:1533–1543.

30. Godin AO, Irisov VG, Charnotskii MI. Passive acoustic measurements of wind velocity and sound speed in air. J Acoust Soc Am. 2014;135:EL68–74.

31. Godin AO. Recovering the acoustic Green's function from ambient noise cross correlation in an inhomogeneous moving medium. Phys Rev Lett. 2006;97:054301.

32. Cheinet S, Ehrhardt L, Broglin T. Impulse source localization in an urban environment: time reversal versus time matching. J Acoust Soc Am. 2016;139:128–140.

33. Albert DG, Liu LB, Moran ML. Time reversal processing for source location in an urban environment. J Acoust Soc. Am. 2005;118:616–619.

34. Hengy S, Hamery P, De Mezzo S, Duffner P. Networked localization of sniper shots using acoustics. Proc of SPIE. 2011;8046:804602.

35. Lui LB, Xie H, Albert DG, Eller PR, Chen JRC. A scenario study for improving cost-effectiveness in acoustic time-reversal source relocation in an urban environment. J Computational Acoustics. 2012;20:124003.

36. Lui LB, Albert DG, Wilson DK. The effect of changing scatter positions on acoustic time-reversal refocusing in a 2D urban environment at low frequencies. J Geophysics and Engineering. 2007;4:276–284.

37. Ostashev VE. Acoustics in moving inhomogeneous media. London (UK): E & FN SPON; 1997.

38. Ostashev VE, Wilson DK, Liu L, Aldridge DF, Symons NP, Marlin D. Equations for finite-difference, time-domain simulation of sound propagation in moving inhomogeneous media and numerical implementation. J Acoust Soc Am. 2005;117:503–517.

39. Brooks LA, Gerstoft P. Green's function approximation from cross-correlation of active sources in the ocean. J Acoust Soc Am. 2009;126:46–55.

40. Campillo M, Paul A. Long-range correlations in the diffuse seismic coda. Science. 2003;299:547–9.

41. Gerstoft P, Sabra KG, Roux P, Kuperman W, Fehler MC. Green's functions extraction and surface-wave tomography from microseisms in southern California. Geophysics. 2006;71:SI23–SI31.

42. Derode A, Larose E, Tanter M, De Rosny J, Tourin A, Campillo M. Recovering the Green's function from field-field correlations in an open scattering medium (L). J Acoust Soc Am. 2003;113:2973–6.

43. Fan Y, Snieder R. Required source distribution for interferometry of waves and diffusive fields. Geophysical J Intl. 2009;179:1232–44.

44. Wapenaar K, Fokkema J. Green's function representations for seismic interferometry. Geophysics. 2006;71:SI33–SI46.

45. Halliday D, Curtis A Seismic interferometry, surface waves and source distribution. Geophysical J Intl. 2008;175:1067–87.

46. Cobden L, Tong C, Warner M. Influence of acoustic source density on cross-correlated signals: Implications for amplitude-based tomography in helioseismology. Astrophysical J. 2010;725:313.

47. Wapenaar K, Van Der Neut J, Ruigrok E, Draganov D, Hunziker J, Slob E, et al. Seismic interferometry by crosscorrelation and by multidimensional deconvolution: a systematic comparison. Geophysical J Intl. 2011;185:1335–64.

48. Mulargia F. The seismic noise wavefield is not diffuse. J Acoust Soc Am. 2012;131:2853–8.

49. Tsai VC. On establishing the accuracy of noise tomography travel-time measurements in a realistic medium. Geophysical J Intl. 2009;178:1555–64.

50. Kao H, Behr Y, Currie CA, Hyndman R, Townend J, Lin FC, et al. Ambient seismic noise tomography of Canada and adjacent regions: part I. crustal structures. Journal of Geophysical Research: Solid Earth. 2013;118:5865–87.

51. Van Wijk K. On estimating the impulse response between receivers in a controlled ultrasonic experiment. Geophysics. 2006;71:SI79–SI84.

52. Alberts WCK, Sanchez KJ. Deduction of the acoustic impedance of the ground via a simulated three-dimensional microphone array. J Acoust Soc Am. 2013;134:EL471–EL476.

List of Symbols, Abbreviations, and Acronyms

1-D	1-dimensional
2-D	2-dimensional
AGL	above ground level
CC	cross correlation
IQR	interquartile range
ISR	intelligence, surveillance, and reconnaissance
MDD	multidimentional deconvolution
PSF	point-spread function
SNR	signal-to-noise ratio
UTC	Coordinated Universal Time

1	DEFENSE TECHNICAL
(PDF)	INFORMATION CTR
	DTIC OCA
2	DIR ARL
(PDF)	IMAL HRA
	RECORDS MGMT
	RDRL DCL
	TECH LIB
1	GOVT PRINTG OFC
(PDF)	A MALHOTRA
1	GOVT PRINTG OFC
(PDF)	A MALHOTRA
4	ERDC
(PDF)	G LYONS
	M SWEARINGEN
	D K WILSON
	M WHITE
1	UNIV COLORADO
(PDF)	V OSTASHEV
1	UNIV MISSISSIPPI
(PDF)	W PRATHER
	R RASPET
14	ARL
(PDF)	RDRL CI
	L SOLOMON
	RDRL CIE
	P CLARK
	RDRL CIE S
	S COLLIER
	M DENIS
	D JAMES
	D LIGON
	J NOBLE
	C WILLIAMSON
	RDRL SES
	A LADAS
	RDRL SES P
	WC KIRKPATRICK ALBERTS II
	C REIFF
	ML SCANLON
	L SIM
	S TENNEY